All of Low-Rank and Sparse: A Recast Total Variation Approach to Hyperspectral Denoising

Haijin Zeng , *Student Member, IEEE*, Shaoguang Huang , *Member, IEEE*, Yongyong Chen , *Member, IEEE*,
Hiep Luong , and Wilfried Philips , *Senior Member, IEEE*

Abstract—**Hyperspectral image (HSI) processing tasks frequently rely on spatial–spectral total variation (SSTV) to quantify the local smoothness of image structures. However, conventional SSTV only considers a sparse structure of gradient maps computed along the spatial and spectral dimensions while neglecting other correlations. To address this limitation, we introduce low-rank guided SSTV (LRSTV), which characterizes the sparsity and low-rank priors of the gradient map simultaneously. First, we verify through numerical tests and theoretical analyses that the gradient tensors are not only sparse but also low-rank. Subsequently, to model the low rankness of the gradient map, we use the tensor average rank to represent the low Tucker rank of gradient tensors. The convex envelope of the tensor average rank is then employed to penalize the rank on the gradient map after the Fourier transform along the spectral dimension. By naturally encoding the sparsity and low-rank priors of the gradient map, LRSTV results in a more accurate representation of the original image. Finally, we demonstrate the effectiveness of LRSTV by integrating it into the HSI processing model, replacing conventional SSTV, and testing it on two public datasets with nine cases of mixed noise and two datasets with realistic noise. The results show that LRSTV outperforms conventional SSTV in terms of accuracy and robustness.**

Index Terms—**Hyperspectral images (HSIs), restoration, spatial–spectral, total variation (TV).**

I. INTRODUCTION

THREE-DIMENSIONAL hyperspectral images (HSIs) boast exceptional spectral accuracy, outstripping traditional imaging systems. Thanks to their ability to incorporate many spectral bands, HSIs can reveal material properties and facilitate various image analysis tasks, including face recognition, mineral exploration, target detection, and quality control [1]. However, real-world imaging conditions—such as weather, sensor sensitivity, photon effects, and lighting conditions—can lead to a range of degradations in HSIs that seriously impact subsequent processing [2], particularly when it comes to noise. Therefore, an effective recovery algorithm is essential for improving the accuracy of subsequent HSI processing.

HSI denoising, i.e., estimating a clean HSI from a noisy one, is essentially an inverse problem. Regularization is one of the most effective and widely used methods to solve this kind of inverse problem. One of the key components of this method is to explore and encode the prior structure and constrain the solution space accordingly, in the form of a regularization term. Regularization technology based on spatial–spectral total variation (SSTV) is a widely used and most effective and powerful image restoration method. SSTV explores the local smoothness (in most pixels) along the HSI spatial and spectral directions. The spatial local smoothness means that similar objects/shapes are usually distributed adjacently with similar spectral waves. Moreover, sensor data from adjacent spectral bands tend to have some correlation, e.g., because the spectral filters in the sensors have overlapping bandpass characteristics similarity [3]. It should be noted, however, that spectra also contain important narrow peaks and valleys. These properties lead to piecewise smoothness, which translates into a low total variation (TV). The local smooth prior structure possessed by HSI can be equivalently characterized as the sparsity of the gradient map calculated along the spatial and spectral modes of the HSI and, then, naturally embedded as the TV of the different modes of the HSI.

The TV regularization method has been widely used for image restoration and has been successful in achieving good results. However, it has some limitations in exploring the structures of HSI beyond sparsity. The SSTV method, based on the L_1 norm, only captures sparsity in the gradient domain, assuming that the sparsity in all bands of the gradient maps is independent. This assumption does not reflect the actual HSI scene, as the original HSI and its gradient map exhibit spectral band correlation and low rankness. To address this limitation, we propose a novel low-rank guided total variation regularization (LRSTV) term that integrates both sparsity and low rankness of the gradient map along all HSI bands. Compared to the conventional SSTV, the proposed LRSTV represents additional low-rank features of the gradient map and can replace SSTV to improve the performance of the general HSI processing models. We demonstrate the low rankness of the gradient map through numerical testing and theoretical analysis. Furthermore, we propose an LRSTV regularized tensor low-rank decomposition model for HSI denoising and

Haijin Zeng, Hiep Luong, and Wilfried Philips are with the Image Processing and Interpretation, imec Research Group, Ghent University, 9000 Gent, Belgium (e-mail: haijin.zeng@ugent.be; hiep.luong@ugent.be; wilfried.philips@ugent.be).

Shaoguang Huang is with the School of Computer Science, China University of Geosciences, Wuhan 430074, China (e-mail: huangshaoguang@cug.edu.cn).

Yongyong Chen is with the School of Computer Science and Technology, Harbin Institute of Technology Shenzhen, Shenzhen 518055, China (e-mail: yongyongchen.cn@gmail.com).

conduct comprehensive experiments on both simulated and real data. The results confirm the superiority of the proposed model over existing technologies and demonstrate the promising performance improvement that can be achieved by easily replacing traditional SSTV with LRSTV. The contributions of this article are listed as follows.

1) We propose a novel low-rank guided total variation regularization (LRSTV), which integrates the sparsity and low rankness of the gradient map.
2) We have fully verified the fact that the gradient map of the image is not only sparse but also (approximately) low-rank from both numerical testing and theoretical analysis.
3) We propose an LRSTV regularized tensor low-rank decomposition model for HSI denoising.

The rest of this article is organized as follows: Section II reviews studies relevant to low-rank-based methods and TV regularized low-rank models. Section III proposes the LRSTV regularization term, a low-rank denoising model based on it, and an ADMM-based optimization algorithm is designed. Simulated and real HSI data experiments verify the performance of the proposed model in Section IV. Finally, Section V concludes this article.

II. RELATED WORK

One of the simple techniques for HSI denoising involves denoising each band independently. This approach utilizes traditional 1-D or 2-D denoising methods designed for natural images and applies them to HSI denoising. Since each pixel of HSI can be considered a 1-D signal, it can be denoised, and each spectral band of HSI can be treated as a grayscale image and denoised accordingly. However, these methods fail to account for the strong correlation present in the spectral or spatial directions in HSI, leaving ample room for model performance improvement.

To address this limitation, recent research has focused on extending 1-D or 2-D denoising models to 3-D models that can explore spatial and spectral information simultaneously, leading to better outcomes than band-by-band denoising techniques. Zhang et al. [4] proposed a recovery model based on Bayesian theory that averages HSI spectral bands to generate potential multispectral images. Additionally, Xue et al. [5] and Wang et al. [6] introduced sparsity-based low-rank decomposition methods that effectively represent structured sparsity and low-rank priors, resulting in promising results.

Nonlocal self-similarity is a widely used prior information in HSI processing [7], [8]. It means that for any image block of HSI in space, a similar texture or structure can always be found in the entire image. For the HSI of each band, the nonlocal similarity block reveals the low rank of the spatial dimension. Therefore, by exploring this low rankness, the spatial noise can be significantly alleviated. BM4D [9] is a classic method of encoding this nonlocal prior. Similar to the block technique in BM4D, Zhang et al. [10] propose to divide the HSI into overlapping small blocks and then rank them into a matrix

band by band, and finally use a low matrix to approximate the restoration of the potential image. Furthermore, a nonlocal model that exploits the intra and interpatch correlation is proposed in [11]. To increase the approximate accuracy of low-rank matrices, Chen et al. [12] proposed a nonconvex γ norm instead of the nuclear norm in LRMR and proposed the NonLRMA model. Zha et al. [13] proposed a series of work about rank residual constraints. Furthermore, rank metrics can also be integrated with group sparsity for image restoration, e.g., [14], [15], [16], [17], [18]. In addition, based on the plug-and-play (PnP) framework, Zeng et al. [19] proposed the NLRPnP model, which can simultaneously represent the local low-rank structure and nonlocal self-similarity of HSI. Powered by a deep model, the low-rank tensor-decomposition-based traditional iteration denoising model is extended by a PnP deep prior network [20], which boosts the performance on Gaussian denoising.

Recent studies have demonstrated the superiority of tensor-based restoration methods over matrix-based methods [21]. One advantage of tensor methods is that they can model the 3-D HSI directly while matrix methods require the HSI to be unfolded into 2-D data, leading to loss or destruction of some structural information. Tensor decomposition or approximation can represent the low-rank structure of HSI in the tensor framework [22], [23], [24]. Several widely used tensor-based methods include Tucker decomposition and Tucker rank, CP decomposition and CP rank, T-SVD decomposition and tubal rank, average rank, tensor train, and tensor ring [25], [26], [27]. In [28], nonlocal low-rank and CP tensor decomposition are combined to represent global spectral correlation and spatial nonlocal self-similarity. To achieve an accurate estimation of the Tucker rank, Tian et al. [29] introduce a constraint on the latent factors of Tucker decomposition using the nuclear norm. This constraint alleviates the burden associated with rank selection. Additionally, Zeng et al. [20] introduce a deep network with Tucker-based low-rank prior into the PnP framework to propose a deep PnP regularized HSI restoration model, which achieves promising results. Xu et al. [30] propose a redesigned deep sparse representation network that makes the sparse-based model competitive again.

TV regularization is a powerful method for image restoration that effectively captures the local smoothness of an image. It can be easily incorporated into low-rank matrix or tensor-based image restoration frameworks as a regularizer for representing smoothness prior. TV achieves sparsity of the gradient map of an image by utilizing either L_1 norm (anisotropic TV) or L_2 norm (isotropic TV). Numerous models for HSI restoration have been developed using TV, such as those presented in [3] and [31], which have been shown to effectively improve the model's performance.

In addition, several alternative regularization terms to TV have also been proposed, including l_p quasi-parameterization [32] and $l_1 - \alpha l_2$ parameterization of the gradient map [33]. The classical TV is essentially a first-order gradient, and higher-order generalized TV (TGV) [34] has been developed to capture intensity variations of the smoothed region more accurately while maintaining edge details and reducing artifacts, although with high computational complexity [35]. While 2-D TV has shown powerful capabilities in natural image processing, it has been

extended to the 3-D case [36] for use in HSI, video, multispectral images, and MRI image processing. For instance, Zeng et al. [37] propose a nonconvex 3-D TV that utilizes an $L_1 - \alpha L_2$ metric to encode sparsity, improving gradient map sparsity representation for HSI. Furthermore, an enhanced TV has been proposed in [3] that defines regularization under a linear transform. Zhang et al. [38] and Wang et al. [39] have proposed two hybrid TV methods that enhance the modeling of HSI smoothness. Because of TV's simplicity and convexity, it can be easily combined with other regularization terms into a unified model to enhance HSI restoration algorithm performance, as demonstrated in [37], [40], and [41], among others. However, TV-based regularization does not fully exploit image similarity, particularly in HSI where spectral correlation is significant.

III. HSI RESTORATION VIA A LRSTV REGULARIZED TENSOR DECOMPOSITION

A. Proposed LRSTV Regularization

The regularization technology based on the TV has been regarded as a powerful image restoration method. It can effectively preserve the spatial sparsity in addition to protecting the boundary information of the image. TV has two mathematical definitions, i.e.,

$$\|\mathbf{X}\|_{\text{TV}}^{\text{iso}} := \sum_{i=1}^{mn} \sqrt{\left(\mathrm{D}_1^i \mathbf{X}\right)^2 + \left(\mathrm{D}_2^i \mathbf{X}\right)^2}$$

$$\|\mathbf{X}\|_{\text{TV}}^{\text{ani}} := \sum_{i=1}^{mn} \left|\mathrm{D}_1^i \mathbf{X}\right| + \left|\mathrm{D}_2^i \mathbf{X}\right| \tag{1}$$

where $\mathbf{X} \in \mathbb{R}^{m \times n}$; $\mathrm{D}_1^i, \mathrm{D}_2^i$ denote the gradient operator along horizontal and vertical directions at pixel i. Subsequently, 2-D TV was expanded to 3-D and widely used in HSI processing. The widely used and worked sparsity measure designed for gradient map is the SSTV, i.e., using L_1-norm metric to measure sparsity [40]

$$\|\mathcal{L}\|_{\text{SSTV}}^{\text{ani}} = \tau_1 \|\mathcal{D}_1 \mathcal{L}\|_1 + \tau_2 \|\mathcal{D}_2 \mathcal{L}\|_1 + \tau_3 \|\mathcal{D}_3 \mathcal{L}\|_1 \tag{2}$$

where $\mathcal{L} \in \mathbb{R}^{m \times n \times p}$ denotes an HSI, $\mathcal{D}_3$ is the additional gradient operator along the spectral direction, and τ_1, τ_2, τ_3 are nonnegative regularization parameters.

Mathematically, SSTV regularization, i.e., 3-D anisotropic TV, measures the sparsity of the gradient map by utilizing L_1 norm as the convex approximation of L_0 norm. This metric has achieved great success in many tasks of image processing. However, we noticed one thing that, in SSTV, only sparsity is explored. Here, we cannot help but want to ask questions: Is the gradient map only sparse? Is there no other prior information that can be explored? According to the linear mixture model of HSI, one can represent each spectral feature by using a linear combination of a small number of pure spectral end members. Especially, let $\mathbf{L}_{(3)}$ denotes the mode-3 matrix of HSI $\mathcal{L}$, $\mathbf{H} \in \mathbb{R}^{p \times r}$ represents the endmember matrix, and $\mathbf{P} \in \mathbb{R}^{mn \times r}$ denotes the abundance matrix. Then, we have $\mathbf{L}_{(3)} = \mathbf{P}\mathbf{H}^T$, and $r \ll p$ or $r \ll mn$ [25], [40], which shows that the number of end members r is relatively small than mn and p. This means

that only a few of the singular values of $\mathbf{L}_{(3)}$ are nonzero. Taking Pavia as an example, as shown in Fig. 2, the singular value curve of $\mathbf{L}_{(3)}$ decays rapidly. Furthermore, in Fig. 2, one can also see that both the singular value curves of $\mathbf{L}_{(1)}$ and $\mathbf{L}_{(2)}$ also decay rapidly. In summary, all the three modes of HSI have similar low rankness. Next, we will show this low-rank structure that appears in the image domain will also be inherited by the gradient map of the original image, and verify it from both numerical testing and theoretical analysis.

Numerical testing: Fig. 1(a) displays a real 3-D HSI cube, expressed as $\mathcal{L} \in \mathbb{R}^{200 \times 200 \times 160}$; (b) shows the difference operator along the spatial height, width, and spectral direction; (c) represents the gradient maps of the original HSI in spatial vertical, horizontal, and spectral directions are expressed as $\mathcal{G}_n \in \mathbb{R}^{200 \times 200 \times 160}, n = 1, 2, 3$. Each tensor is stacked by a gradient map of 160 slices. Except for the sparsity shown in Fig. 1(g). It can be seen from Fig. 1(f) that although the sparsity in different bands of the gradient map is not the same or even independent, there is a clear correlation between the different bands of the HSI gradient map. Furthermore, Fig. 1(d) shows the gradient map in the Fourier domain. Compared with the original gradient map, one can see that the low rankness of the gradient map in the Fourier domain is more obvious, especially the gradient map in two directions of spatial dimension. Due to the fact that most of the singular values are small and close to 0, only a few singular values have large values.

Theoretical analysis: In fact, gradient transformation hardly changes the rank of the original image, i.e., the gradient map inherits the low rankness of the original image in the image domain. Next, we prove this conclusion theoretically.

Theorem 4.1: Given any 3-D HSI $\mathcal{L} \in \mathbb{R}^{m \times n \times p}$ and its gradient tensors $\mathcal{D}_x \mathcal{L}, \mathcal{D}_y \mathcal{L}, \mathcal{D}_z \mathcal{L} \in \mathbb{R}^{m \times n \times p}$, we have

$$r_{tc}\left(\mathcal{D}_x \mathcal{L}\right) \approx r_{tc}\left(\mathcal{D}_y \mathcal{L}\right) \approx r_{tc}(\mathcal{L}) \approx r_{tc}\left(\mathcal{D}_z \mathcal{L}\right) \tag{3}$$

where the Tucker rank of $\mathcal{A}$ is defined as $r_{tc}(\mathcal{A}) = (r(\mathbf{A}_{(1)}), r(\mathbf{A}_{(2)}), r(\mathbf{A}_{(3)}))$, and $r(\mathbf{A}_{(i)})$ is the rank of mode-i matricization of $\mathcal{A}$.

Proof: Due to the three modes in multitubal rank having equivalent status, we first prove the theorem in one model; then, it can easily be deduced to the remaining two modes. Then, we have

$$r_{tc}(\mathcal{L}) = \left(r(\mathbf{L}_{(1)}), r(\mathbf{L}_{(2)}), r(\mathbf{L}_{(3)})\right)$$

$$r_{tc}(\mathcal{D}_x \mathcal{L}) = \left(r(\mathcal{D}_x \mathbf{L}_{(1)}), r_2(\mathcal{D}_x \mathbf{L}_{(2)}), r_3(\mathcal{D}_x \mathbf{L}_{(3)})\right) \tag{4}$$

To prove $r_{tc}(\mathcal{D}_x \mathcal{L}) \approx r_{tc}(\mathcal{L})$, one only need to prove that $r(\mathcal{D}_x \mathbf{L}_{(i)}) \approx r(\mathbf{L}_{(i)}), i = 1, 2, 3$. Let $\mathcal{D}_x \mathbf{L}_{(1)} = \mathbf{D}_x \mathbf{L}_{(1)}$, where $\mathbf{D}_x \in \mathbb{R}^{np \times np}$ is the circulant matrix corresponding to the forward finite difference operator $\mathcal{D}_x$ with periodic boundary conditions along the x-axis. Then, we know that $r(\mathbf{D}_x) = np - 1$. To prove that

$$r\left(\mathbf{L}_{(1)}\right) - 1 \le r\left(\mathcal{D}_x \mathbf{L}_{(1)}\right) \le \min\{np - 1, r(\mathbf{L}_{(1)})\} \le r\left(\mathbf{L}_{(1)}\right) \tag{5}$$

i.e., $r(\mathcal{D}_x \mathbf{L}_{(1)}) \approx r(\mathbf{L}_{(1)})$. First, we prove that $r(\mathcal{D}_x) + r(\mathbf{L}_{(1)}) - np \le r(\mathcal{D}_x \mathbf{L}_{(1)})$. Let $r(\mathcal{D}_x) = r_1$, $r(\mathbf{L}_{(1)}) = r_2$, $r(\mathcal{D}_x \mathbf{L}_{(1)}) = r$; then, there are invertible matrices $\mathcal{D}_x$ and $\mathbf{L}_{(1)}$
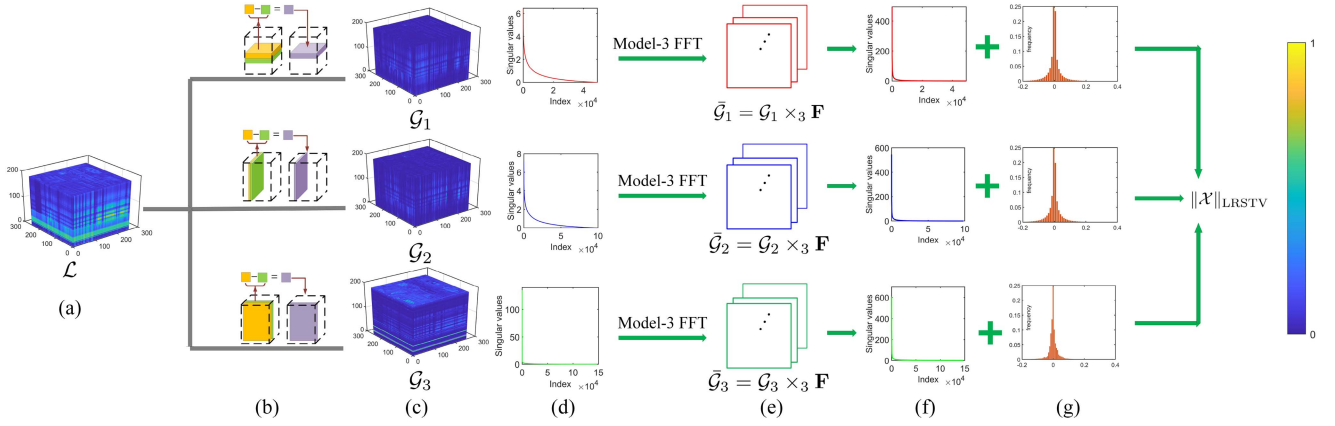
Fig. 1. Illustration of the proposed LRSTV regularization terms. (a) Example of real HSI data *HYDICE Washington DC Mall*, represented as a tensor $\mathcal{L}$. (b) Illustrations of the difference operators along the spatial height, width, and spectral modes, respectively. (c) Gradient maps of $\mathcal{L}$ in spatial height, width, and spectrum, represented as $\mathcal{G}_n, n = 1, 2, 3$, respectively. Each of these tensors is stacked by 160 slices of gradient maps. (d) Singular value curves of the gradient maps. (e) FFT-transformed gradient maps, $\mathbf{F}$ denotes a Fourier transform matrix. (f) Singular value curves of FFT-transformed gradient maps. (g) Frequency distributions of the gradient maps of *HYDICE Washington DC Mall* data.
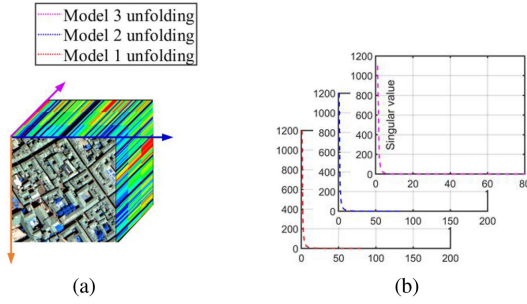

Fig. 2. (a) Real HSI cube of Pavia Centre. (b) Singular values of its model-$n(n = 1, 2, 3)$ unfolding matrix. From the figure, one can see that the third-order real HSI is obviously correlated along its three modes.

such that the following equation holds:

$$\mathbf{P}\mathcal{D}_x\mathbf{Q} = \begin{bmatrix} \mathbf{E_{r_1}} & \mathbf{0} \\ \mathbf{0} & \mathbf{0} \end{bmatrix}. \tag{6}$$

Let $\mathbf{Q}^{-1}\mathbf{L}_{(1)} = \begin{bmatrix} \mathbf{L}_{r_1 \times m} \\ \mathbf{L}_{(n-r_1) \times m} \end{bmatrix}$, we have

$$r = r\left(\mathcal{D}_x\mathbf{L}_{(1)}\right) = r\left(\mathbf{P}\mathcal{D}_x\mathbf{Q}\mathbf{Q}^{-1}\mathbf{L}_{(1)}\right)$$

due to

$$\mathbf{P}\mathcal{D}_x\mathbf{Q}\mathbf{Q}^{-1}\mathbf{L}_{(1)} = \begin{bmatrix} \mathbf{E_{r_1}} & \mathbf{O} \\ \mathbf{O} & \mathbf{O} \end{bmatrix} \begin{bmatrix} \mathbf{L}_{r_1 \times m} \\ \mathbf{L}_{(n-r_1) \times m} \end{bmatrix} = \begin{bmatrix} \mathbf{L}_{r_1 \times m} \\ \mathbf{0} \end{bmatrix}$$

we have $r(\mathbf{L}_{r_1 \times m}) = r(\mathcal{D}_x\mathbf{L}_{(1)}) = r$; however, $r(\mathbf{Q}^{-1}\mathbf{L}_{(1)}) = r_2$, this means that the number of linearly independent rows in $\mathbf{L}_{(n-r_1) \times m}$ is $r_2 - r$, and the total number of rows is $n - r_1$. Therefore, $r_2 - r \leq n - r_1$, that is, $r \geq r_1 + r_2 - n$. Second, to prove that $r(\mathcal{D}_x\mathbf{L}_{(1)}) \leq \min\{r(\mathcal{D}_x), r(\mathbf{L}_{(1)})\}$, we only need to prove $r(\mathcal{D}_x\mathbf{L}_{(1)}) \leq r(\mathcal{D}_x)$ and $r(\mathcal{D}_x\mathbf{L}_{(1)}) \leq r(\mathbf{L}_{(1)})$ at the same time, which can be easily verified.

Similarly, we have

$$\begin{cases} r\left(\mathbf{L}_{(2)}\right) - 1 \leq r\left(\mathcal{D}_y\mathbf{L}_{(2)}\right) \leq r\left(\mathbf{L}_{(2)}\right) \\ r\left(\mathbf{L}_{(3)}\right) - 1 \leq r\left(\mathcal{D}_y\mathbf{L}_{(3)}\right) \leq r\left(\mathbf{L}_{(3)}\right) \end{cases} \tag{7}$$

and $r(\mathcal{D}_y\mathbf{L}_{(2)}) \approx r(\mathbf{L}_{(2)}), r(\mathcal{D}_z\mathbf{L}_{(3)}) \approx r(\mathbf{L}_{(3)})$. Therefore, we get that

$$\begin{cases} r(\mathcal{D}_x\mathbf{L}_{(1)}) \approx r(\mathbf{L}_{(1)}) \\ r(\mathcal{D}_y\mathbf{L}_{(2)}) \approx r(\mathbf{L}_{(2)}) \\ r(\mathcal{D}_z\mathbf{L}_{(3)}) \approx r(\mathbf{L}_{(3)}) \end{cases} \tag{8}$$

And for the forward finite difference operators $\mathcal{D}_x, \mathcal{D}_y, \mathcal{D}_z$ with zero boundary conditions $(r(\mathbf{D}_x) = np - 1, r(\mathbf{D}_y) = mp - 1, , r(\mathbf{D}_z) = mn - 1)$ and symmetric boundary conditions

$$r\left(\mathbf{D}_x\right) = np, r\left(\mathbf{D}_y\right) = mp, , r\left(\mathbf{D}_z\right) = mn \tag{9}$$

we also have the conclusion (8). Therefore, the ranks of $\mathcal{D}_x\mathbf{L}_{(1)}$, $\mathcal{D}_y\mathbf{L}_{(2)}$, and $\mathcal{D}_z\mathbf{L}_{(3)}$ represent the ranks of $\mathbf{L}_{(1)}, \mathbf{L}_{(2)}, \mathbf{L}_{(3)}$, respectively.

From the above numerical tests and theoretical analysis, we get the fact that the gradient map of HSI is not only sparse but also has a low-rank structure, as long as the original HSI is low-rank. For the HSI to be focused in this article, it is worth noting that the low rankness along the spectral dimension is much more obvious than that of the spatial dimension. Based on these facts, we propose a novel TV regularization to simultaneously characterize the sparsity and low-rank priors of the gradient map. Specifically, the proposed isotropic LRSTV and anisotropic LRSTV are defined as follows:

$$\|\mathcal{L}\|_{\text{LRSTV}}^{\text{ani}} = \sum_{n=1}^{3} \left(\tau_n \|D_n\mathcal{L}\|_1 + \alpha_n r_{tc}(D_n\mathcal{L})\right) \tag{10}$$

$$\|\mathcal{L}\|_{\text{LRSTV}}^{\text{iso}} = \sqrt{\sum_{n=1}^{3} \tau_n \|D_n\mathcal{L}\|_2^2} + \sum_{n=1}^{3} \alpha_n r_{tc}(D_n\mathcal{L}) \tag{11}$$

where τ_n and α_n are nonnegative regularization parameters. Then, the key issue is to find a simple method to estimate Tucker rank. Here, we utilize the new average rank to represent the low rankness that exists in the gradient map, i.e., replacing $r_{tc}(D_n\mathcal{L})$ in (10) and (11) with $r_a(D_n\mathcal{L})$, where $r_a(\mathcal{A}) =$

$\frac{1}{n_3}$ rank(bcirc($\mathcal{A}$)), and bcirc($\mathcal{A}$) $\in \mathbb{R}^{n_1 n_3 \times n_2 n_3}$ is the block circulant matrix of $\mathcal{A}$ defined as follows:

$$\text{bcirc}(\mathcal{A}) = \begin{bmatrix} \mathbf{A}^{(1)} & \mathbf{A}^{(n_3)} & \cdots & \mathbf{A}^{(2)} \\ \mathbf{A}^{(2)} & \mathbf{A}^{(1)} & \cdots & \mathbf{A}^{(3)} \\ \vdots & \vdots & \ddots & \vdots \\ \mathbf{A}^{(n_3)} & \mathbf{A}^{(n_3-1)} & \cdots & \mathbf{A}^{(1)} \end{bmatrix} \quad (12)$$

where $\mathbf{A}^{(i)} := \mathcal{A}(:,:,i)$ is the ith front slice of $\mathcal{A}$.

B. Approximation of the LRSTV

Actually, there are some connections between tensor Tucker rank and average rank, and these properties imply that the low Tucker rank or low average rank assumptions are reasonable for their applications in real visual data [42]. Let $r_{\text{tc}}(\mathcal{A}) = \left(r\left(\mathbf{A}_{(1)}\right), r\left(\mathbf{A}_{(2)}\right), r\left(\mathbf{A}_{(3)}\right)\right)$, where $\mathbf{A}_{(i)}$ denotes the mode-i matricization of $\mathcal{A}$, be the Tucker rank of $\mathcal{A}$. Then, we have $r_{\text{a}}(\mathcal{A}) \leq r(\mathbf{A}_{(1)})$, i.e., if a tensor with low Tucker rank, it also has a low average rank; furthermore, the low average rank hypothesis is weaker than the low rank hypothesis [42], [43]. Therefore, one can use tensor average rank to represent the low Tucker rank in (10) and (11). Furthermore, with tensor average rank we have the following theorem.

Theorem 4.2 ([44]): On the set $\{\mathcal{A} \in \mathbb{R}^{n_1 \times n_2 \times n_3} \mid \|\mathcal{A}\| \leq 1\}$, $\mathcal{A} = \mathcal{U} * \mathcal{S} * \mathcal{V}^*$ represents the t-SVD of $\mathcal{A} \in \mathbb{R}^{n_1 \times n_2 \times n_3}$. The tensor tubal rank $r_t(\mathcal{A})$ is defined as the number of nonzero singular tubes of $\mathcal{S}$, i.e., $r_t(\mathcal{A}) = \#\{i, \mathcal{S}(i,i,:) \neq \mathbf{0}\}$. The tensor nuclear norm of $\mathcal{A}$ is defined as $\|\mathcal{A}\|_* := \langle \mathcal{S}, \mathcal{I} \rangle = \sum_{i=1}^{r} \mathcal{S}(i,i,1)$, $r = r_t(\mathcal{A})$. Then, the convex envelope of the tensor average rank $r_a(\mathcal{A})$ is the tensor nuclear norm $\|\mathcal{A}\|_*$.

In addition, for the HSI, we focused on, in this article, its spectral correlation is much stronger than spatial dimensions [3], [40]. For example, as shown in Fig. 2, for the Pavia datasets with a size of $200 \times 200 \times 80$, all the singular value curves of mode-1, mode-2, and mode-3 matricizations have obvious decaying trends but the spectral modes have a greater rate of curve drop than spatial modes. By using the HySime algorithm [45], it is estimated the spectral rank is 8 while the empirical spatial rank is 160, which gets the best PSNR and SSIM. Therefore, it is necessary to introduce orientation sensitivity to the low-rank measure. To this end, we mainly represent the low rankness strictly defined along tubal orientation, i.e., model spectral low rankness, by using the tensor nuclear norm proposed in Theorem 4.2, and (10) and (11) can be approximated as follows:

$$\|\mathcal{L}\|_{\text{LRSTV}}^{\text{ani}} = \sum_{n=1}^{3} \left(\tau_n \|D_n \mathcal{L}\|_1 + \alpha_n \|D_n \mathcal{L}\|_* \right) \quad (13)$$

$$\|\mathcal{L}\|_{\text{LRSTV}}^{\text{iso}} = \sqrt{\sum_{n=1}^{3} \tau_n \|D_n \mathcal{L}\|_2^2} + \sum_{n=1}^{3} \alpha_n \|D_n \mathcal{L}\|_* \quad (14)$$

where $\|.\|_*$ represents the new tensor nuclear norm, $D_n, n = 1, 2, 3$ denote the gradient operator. The proposed LRSTV can be regarded as a generalization of classic SSTV, that is, SSTV is a special case of the proposed LRSTV. When the coefficient λ is 0, LRSTV degenerates to SSTV. It is worth pointing out that the new regularization not only imposes sparsity on the
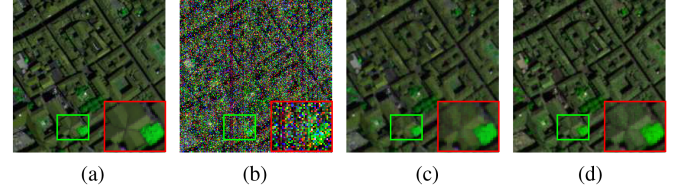

Fig. 3. Effectiveness of the additional low-rank strategy. (a) Original false-color image (R: 31, G: 61, B: 9). (b) Simulated noisy image under zero-mean Gaussian noise, impulse noise, deadline, and stripe (the variance value of Gaussian noise and percentages of impulse noise being randomly selected from 0.1 to 0.2, the width of the deadlines was randomly generated from 1 to 3, the number of stripes being randomly selected from 20 to 40 (PSNR = 11.17 dB). (c) Denoising result of the SSTV method without additional low-rank strategy (PSNR = 31.07 dB). (d) Denoising result of the proposed method with additional low-rank strategy (PSNR = 32.63 dB).

gradient map itself but also calculates low rank on the gradient map after the Fourier transform along the spectral dimension (FFT is contained in $\|.\|_*$). It naturally encodes the sparsity and low-rank priors of the gradient map and, thus, is expected to reflect the inherent structure of the original image more faithfully than common SSTV.

As demonstrated in the previous paragraph, since SSTV only explores the sparsity of the gradient maps, it cannot effectively restore a potentially clean image when the observed one has serious noise pollution. Our LRSTV additionally explores the low-rank prior of the gradient map, which helps to deal with scenarios with heavy noise. Due to image denoising is essentially an inverse problem, the more precise and appropriate the constraints added in the solution space, the closer the approximate solution to the true solution is. In Fig. 3, we give an intuitive comparison between TV models with and without gradient low-rank strategy. Obviously, the local details of Fig. 3(d) are more clear than that of SSTV without gradient low-rank strategy, which shows the effectiveness of low-rank strategy in exploring the prior knowledge of the gradient map.

C. Low-Rank Tensor Decomposition With Anisotropic LRSTV

Furthermore, it is important to note that in addition to the previously mentioned sparse and low-rank priors of the gradient map, the third-order HSI possesses inherent structural information in both its spatial and spectral modes within the image domain [40]. While the LRSTV method successfully captures the low rankness of HSI in the gradient domain, the proposed algorithm takes a significant stride forward by incorporating low-rank tensor decomposition to effectively model the low rankness of HSI in the image domain. This advanced approach enables the algorithm to comprehensively capture and represent the low-rankness characteristics of HSI in both the image and gradient domains. Consequently, the proposed method provides a dual-domain representation, ensuring a more holistic understanding and utilization of the low-rankness properties inherent in HSI data. Here, Tucker decomposition is employed to represent the spatial–spectral low rankness of HSIs displayed in Section III-A. By using the Tucker-3 decomposition, any third-order tensor $\mathcal{L} \in \mathbb{R}^{m \times n \times p}$ with multilinear rank (r_1, r_2, r_3) can

be decomposed as follows:

$$\mathcal{L} = \mathcal{C} \times_1 \mathbf{U}_1 \times_2 \mathbf{U}_2 \times_3 \mathbf{U}_3, \mathbf{U}_i^T \mathbf{U}_i = \mathbf{I}, i = 1, 2, 3 \quad (15)$$

where $\mathcal{C}$ denotes the factor tensor, i.e., the so-called core tensor; $\mathbf{U}_i$ is the ith factor matrix, which has rank $r_i, i = 1, 2, 3$. Finally, by combining the correlation between the spatial mode and the spectral mode, the low rank and sparse structure of the gradient map, we propose LRSTV regularized tensor decomposition (named TDLRSTV) model, i.e.,

$$\min_{\mathcal{L}, \mathcal{S}} \|\mathcal{L}\|_{\text{LRSTV}}^{\text{ani}} + \lambda \|\mathcal{S}\|_1$$

$$\text{s.t.} \quad \mathcal{Y} = \mathcal{L} + \mathcal{S}$$

$$\mathcal{L} = \mathcal{C} \times_1 \mathbf{U}_1 \times_2 \mathbf{U}_2 \times_3 \mathbf{U}_3, \mathbf{U}_i^T \mathbf{U}_i = \mathbf{I}, i = 1, 2, 3. \quad (16)$$

D. Optimization Procedure

In this section, we design an algorithm based on ALM and ADMM [40] to solve the proposed TDLRSTV. First, we introduce three auxiliary variables to split the multiple regularization terms applied on $\mathcal{L}$. In addition, to simplify, we set the same τ_n and α_n for all n and denote them as τ, α, respectively, and let $D_w(\cdot) = [w_1 \times D_1(\cdot); w_2 \times D_2(\cdot); w_3 \times D_3(\cdot)]$, where w_1, w_2, w_3 are the three weighted parameters added to three L_1 norm of gradient maps. Then, by introducing auxiliary variables $\mathcal{Z}, \mathcal{F}$, and $\mathcal{E}$, (16) can be rewritten as follows:

$$\min_{\substack{\mathcal{C}, \mathbf{U}_i, \mathcal{L}, \\ \mathcal{F}, \mathcal{S}, \mathcal{E}, \mathcal{Z}}} \tau \|\mathcal{F}\|_1 + \alpha \|\mathcal{E}\|_* + \lambda \|\mathcal{S}\|_1$$

$$\text{s.t.} \quad \mathcal{O} = \mathcal{L} + \mathcal{S}, \mathcal{L} = \mathcal{Z}, D_w(\mathcal{Z}) = \mathcal{F}, \mathcal{E} = \mathcal{F}$$

$$\mathcal{L} = \mathcal{C} \times_1 \mathbf{U}_1 \times_2 \mathbf{U}_2 \times_3 \mathbf{U}_3, \mathbf{U}_i^T \mathbf{U}_i = \mathbf{I}. \quad (17)$$

According to the ALM method, we rewrite the objective function of (17) into the following augmented Lagrangian function:

$$L(\mathcal{L}, \mathcal{S}, \mathcal{Z}, \mathcal{F}, \mathcal{E}) = \tau \|\mathcal{F}\|_1 + \alpha \|\mathcal{E}\|_* + \lambda \|\mathcal{S}\|_1$$

$$\langle \Gamma_1, \mathcal{O} - \mathcal{L} - \mathcal{S} \rangle + \langle \Gamma_2, \mathcal{L} - \mathcal{Z} \rangle + \langle \Gamma_3, D_w(\mathcal{Z}) - \mathcal{F} \rangle$$

$$+ \langle \Gamma_4, \mathcal{E} - \mathcal{F} \rangle + \frac{\mu}{2} \left(\|\mathcal{O} - \mathcal{L} - \mathcal{S}\|_F^2 \right.$$

$$\left. + \|\mathcal{L} - \mathcal{Z}\|_F^2 + \|D_w(\mathcal{Z}) - \mathcal{F}\|_F^2 + \|\mathcal{E} - \mathcal{F}\|_F^2 \right) \quad (18)$$

with the constraints: $\mathcal{L} = \mathcal{C} \times_1 \mathbf{U}_1 \times_2 \mathbf{U}_2 \times_3 \mathbf{U}_3, \mathbf{U}_i^T \mathbf{U}_i = \mathbf{I}$, where μ is the penalty parameter, and $\Gamma_i(i = 1, 2, 3)$ are the Lagrange multipliers. Next, we utilized alternating minimization based on ADMM to split (18) into multiple subproblems, then update each variable $\mathcal{L}, \mathcal{Z}, \mathcal{F}, \mathcal{E}, \mathcal{S}$ alternately. In $(k + 1)$th iteration, variables involved in (18) can be updated as follows:

1) *Update $\mathcal{C}, \mathbf{U}_i, \mathcal{L}$:* With the other variables fixed, the subproblem of $\mathcal{L}$ can be reformulated as follows:

$$\min_{\mathbf{U}_i^T \mathbf{U}_i = \mathbf{I}} \mu \left\| \mathcal{C} \times_1 \mathbf{U}_1 \times_2 \mathbf{U}_2 \times_3 \mathbf{U}_3 - \frac{1}{2} \left(\mathcal{O} - \mathcal{S}^{(k)} \right. \right.$$

$$\left. \left. + \mathcal{Z}^{(k)} + \left(\Gamma_1^{(k)} - \Gamma_2^{(k)} \right) \middle/ \mu \right) \right\|_F^2. \quad (19)$$

Based on the HOOI algorithm [46], one can get $\mathcal{C}^{(k+1)}$, and $\mathbf{U}_1^{(k+1)}, \mathbf{U}_2^{(k+1)}$, and $\mathbf{U}_3^{(k+1)}$, then we have

$$\mathcal{L}^{(k+1)} = \mathcal{C}^{(k+1)} \times_1 \mathbf{U}_1^{(k+1)} \times_2 \mathbf{U}_2^{(k+1)} \times_3 \mathbf{U}_3^{(k+1)}. \quad (20)$$

2) *Update $\mathcal{Z}$:* With the other variables fixed, the subproblem of $\mathcal{Z}$ can be reformulated as follows:

$$\mathcal{Z}^{(k+1)} = \underset{\mathcal{Z}}{\arg\min} \left\langle \Gamma_2^{(k)}, \mathcal{L}^{(k+1)} - \mathcal{Z} \right\rangle + \left\langle \Gamma_3^{(k)}, D_w(\mathcal{Z}) \right.$$

$$\left. - \mathcal{F}^{(k)} \right\rangle + \frac{\mu}{2} \left(\left\| \mathcal{L}^{(k+1)} - \mathcal{Z} \right\|_F^2 \right.$$

$$\left. + \left\| D_w(\mathcal{Z}) - \mathcal{F}^{(k)} \right\|_F^2 \right) \quad (21)$$

which can be treated as solving the following linear system:

$$(\mu \mathbf{I} + \mu D_w^* D_w) \mathcal{Z} = \mu \mathcal{L}^{(k+1)} + \mu D_w^* \left(\mathcal{F}^{(k)} \right) + \Gamma_2^{(k)}$$

$$- D_w^* \left(\Gamma_3^{(k)} \right) \quad (22)$$

where D_w^* denotes the adjoint operator of D_w. By using the fast Fourier transform (FFT) method [40], we have

$$\begin{cases} \mathrm{T}_z = \mu \mathcal{L}^{(k+1)} + \mu D_w^* \left(\mathcal{F}^{(k)} \right) + \Gamma_2^{(k)} - D_w^* \left(\Gamma_3^{(k)} \right) \\ \mathrm{P}_z = w_1^2 |\text{fftn}(D_1)|^2 + w_2^2 |\text{fftn}(D_2)|^2 + w_3^2 |\text{fftn}(D_3)|^2 \\ \mathcal{Z}^{(k+1)} = \text{ifftn} \left(\frac{\text{fftn}(\mathrm{T}_z)}{\mu \mathbf{1} + \mu \mathrm{P}_z} \right) \end{cases} \quad (23)$$

where fftn and ifftn indicate fast 3-D Fourier transform and its inverse transform, respectively. $|\cdot|^2$ is the elementswise square, and the division is also performed elementwise.

3) *Update $\mathcal{F}$:* With the other variables fixed, the subproblem of $\mathcal{F}$ can be reformulated as follows:

$$\mathcal{F}^{(k+1)} = \underset{\mathcal{F}}{\arg\min} \tau \|\mathcal{F}\|_1 + \frac{\mu}{2} \left\| \mathcal{F} - \frac{T_1 + T_2}{2} \right\|_F^2 \quad (24)$$

where $T_1 = D_w\left(\mathcal{Z}^{(k+1)}\right) + \frac{\Gamma_3^{(k)}}{\mu}, T_2 = \mathcal{E}^{(k+1)} + \frac{\Gamma_4^{(k)}}{\mu}$. By introducing the so-called soft-thresholding operator:

$$\mathcal{R}_\Delta(\mathbf{x}) = \begin{cases} x - \Delta, & \text{if} \quad \mathbf{x} > \Delta \\ x + \Delta, & \text{if} \quad \mathbf{x} < \Delta \\ 0, & \text{otherwise} \end{cases} \quad (25)$$

where $x \in \mathbb{R}$ and $\Delta > 0$, then we can update $\mathcal{F}^{k+1}$ as

$$\mathcal{F}^{k+1} = \mathcal{R}_{\frac{\tau}{\mu}} \left(\frac{T_1 + T_2}{2} \right). \quad (26)$$

4) *Update $\mathcal{E}$:* With the other variables fixed, the subproblem of $\mathcal{E}$ can be reformulated as follows [42], [47]:

$$\mathcal{E}^{(k+1)} = \underset{\mathcal{E}}{\arg\min} \|\mathcal{E}\|_* + \frac{\mu}{2\alpha} \left\| \mathcal{E} - \left(\mathcal{F} - \frac{\Gamma_4^{(k)}}{\mu} \right) \right\|_F^2$$

Algorithm 1: TDLRSTV for HSI Denoising.

Require: $m \times n \times p$ observed HSI $\mathcal{O}$, stopping criterion ε, and regularization parameters λ, τ, α.

Ensure: Denoised image $\mathcal{L}$;

  1: Initialize: 1st step: Update $\mathcal{L}$, via (20)
        2nd step: Update $\mathcal{Z}$ via (23)
        3rd step: Update $\mathcal{F}$ via (26)
        4th step: Update $\mathcal{E}$ via (27)
        5th step: Update $\mathcal{S}$ via (29)
        6th step: Update $\Gamma_1, \Gamma_2, \Gamma_3$ via (30)
        7th step: Update the parameter via
        $\mu := \min(\rho\mu, \mu_{\max})$
  2: Check the convergence condition
  3: $\max\{\|\mathcal{O} - \mathcal{L}^{k+1} - \mathcal{S}^{k+1}\|_\infty, \|\mathcal{L}^{k+1} - \mathcal{Z}^{k+1}\|_\infty\} \leq \varepsilon$.

$$= \text{SVT}\left(\mathcal{F} - \frac{\Gamma_4^{(k)}}{\mu}, \frac{\alpha}{\mu}\right). \tag{27}$$

5) *Update $\mathcal{S}$:* Similarly, we should consider

$$\mathcal{S}^{(k+1)} = \arg\min_{\mathcal{S}} \lambda\|\mathcal{S}\|_1 + \frac{\mu}{2}\left\|\mathcal{S} - \left(\mathcal{O} - \mathcal{L}^{(k+1)} + \frac{\Gamma_1^{(k)}}{\mu}\right)\right\|_F^2. \tag{28}$$

similar to the update of $\mathcal{F}$, we have

$$\mathcal{S}^{k+1} = \mathcal{R}_{\frac{\lambda}{\mu}}\left(\mathcal{O} - \mathcal{L}^{(k+1)} + \frac{M_1^{(k)}}{\mu}\right). \tag{29}$$

Finally, we update multipliers $\Gamma_i(i = 1, 2, 3)$, according to the ALM

$$\begin{cases} \Gamma_1^{(k+1)} = \Gamma_1^{(k)} + \mu\left(\mathcal{O} - \mathcal{L}^{(k+1)} - \mathcal{S}^{(k+1)}\right) \\ \Gamma_2^{(k+1)} = \Gamma_2^{(k)} + \mu\left(\mathcal{L}^{(k+1)} - \mathcal{Z}^{(k+1)}\right) \\ \Gamma_3^{(k+1)} = \Gamma_3^{(k)} + \mu\left(D_w\left(\mathcal{Z}^{(k+1)}\right) - \mathcal{F}^{(k+1)}\right). \end{cases} \tag{30}$$

E. Time Complexity Analysis

The main per-iteration cost lies in the update of $\mathcal{E}, \mathcal{Z}, \mathcal{F}, \mathcal{S}$. The update of $\mathcal{E}$ requires computing FFT and p SVDs of $m \times n$ matrices. The updates of $\mathcal{S}$ and $\mathcal{N}$ only need to perform basic tensor operations. Thus, the per-iteration complexity is $O\left(mnp\log(p) + m_{(1)}n_{(1)}^2 p\right)$, where $m_{(1)} = \max(m, n)$, $n_{(1)} = \min(m, n)$.

IV. EXPERIMENTAL RESULTS AND DISCUSSION

In this section, we applied the proposed TDLRSTV to both public simulation and real HSI datasets as shown in Fig. 4, and compared the results with that of several state of the arts to evaluate the performance of TDLRSTV.

A. Experimental Setting

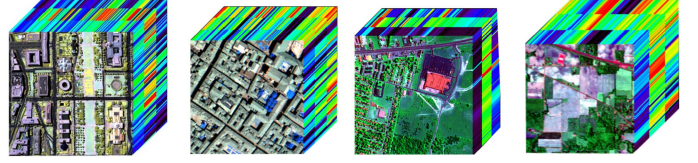*Benchmark Datasets:* Four HSIs datasets are tested.

Fig. 4. Simulation and real HSI datasets tested in the experiments. From left to right: Washington DC Mall dataset, Pavia Centre dataset, HYDICE urban dataset, and AVIRIS Indian Pines dataset.

1) Pavia City Center [48] dataset. The raw Pavia Center dataset has a size of $1096 \times 1096 \times 102$, i.e., there are 102 bands and each band is a 1096×1096 2-D image. After removing the bands heavily polluted by noise, subblock with a size of $200 \times 200 \times 80$ are selected for simulation experiments in this section.

2) Washington DC Mall data [49], the raw data have a size of $1208 \times 307 \times 191$. As [37], subblock with size $256 \times 256 \times 191$ are selected.

3) Indian Pines dataset [49] with size $145 \times 145 \times 220$ was collected by the Airborne Visible Infrared Imaging Spectrometer (AVIRIS). This dataset was selected for real data experiments.

4) HYDICE Urban HSI dataset [50] has the size of $207 \times 207 \times 210$. After deleting the water absorption band, the remaining 189 bands were selected for testing. This dataset was also selected for real data experiments.

Baselines: Ten SOTA HSI denoising methods are employed as the comparison models, i.e., LRTA-based on Tucker decomposition [51], BM4D [9] based on nonlocal self-similarity, LRMR via low-rank matrix approximation [10], LRTV that combines TV and LRMR [41], NAILRMA based on iterative LRMR and noise estimation [52], LRTDTV based on TV and low-rank tensor Tucker decomposition [40], enhanced 3DTV [3], and SSTV [53]. In addition, we also compared the proposed model with deep-learning-based denoising models DPLRTA [20], FFNNet [54], transformer-based SERT [55], and deep-unrolling-based DNA-Net [56].

Evaluation Indexes: To measure the performance of tested models, both qualitative visual evaluation and quantitative index are utilized. Quantitative picture quality indices (PQI): peak signal-to-noise ratio (PSNR), structural similarity (SSIM), and feature similarity (FSIM) [57], which evaluate the quality of the HSI spatial dimension, and erreur relative globale adimensionnelle de synthèse (EGRAS) [58] and spectral angle mapper (SAM) [59], which evaluate the quality of the HSI spectral dimension. The experiments are performed on MATLAB(2019b), Intel core i7@2.2 GHz with 64 GB RAM (Windows), and PyTorch on Linux.

B. Simulated HSI Data Experiments

Mixed noise setting: To simulate HSIs degradation process of noise, nine different noise cases are simulated for the selected HSI datasets. The details are listed as follows.
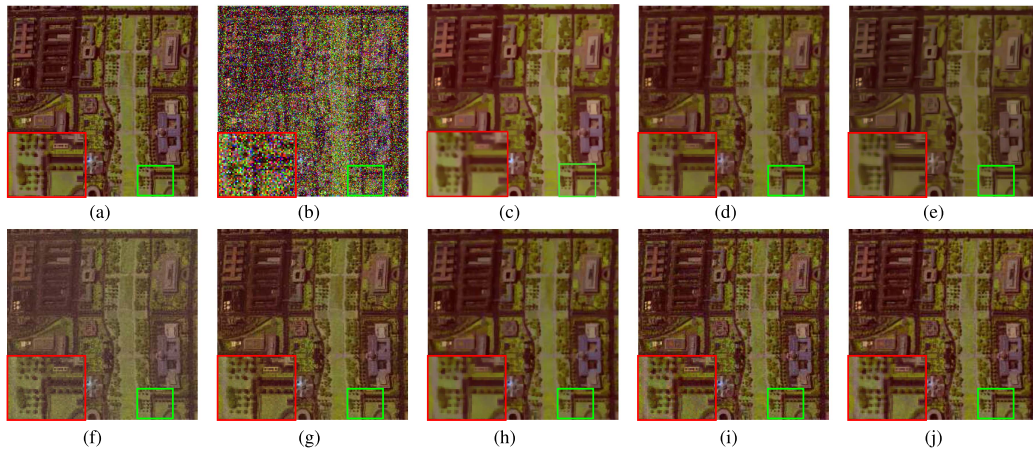
Fig. 5. Recovery performance comparison on the Washington DC Mall data by LRTA, LRTV, BM4D, NAILRMA, LRMR, LRTDTV, SSTV, and the proposed TDLRSTV. The noise level: Gaussian noise (with 0 mean and 0.15 variance) and sparse pepper-and-salt noise (with a percentage of 0.2) are added for all bands; deadlines are added to the 131–160 band, the number of deadlines varies randomly from 3 to 10, and the width of deadlines varies randomly from 1 to 3; stripes are added to the 111–140 band, where the number of bands varies randomly between 20 and 40. The color image is composed of bands 58, 85, and 155 for the red, green, and blue channels, respectively. (a) Original image. (b) Noisy one (10.91 dB). (c) E3DTV (29.85 dB). (d) LRTV (28.35 dB). (e) BM4D (26.41 dB). (f) NALRMA (22.29 dB). (g) LRMR (28.87 dB). (h) LRTDTV (28.78 dB). (i) SSTV (29.05 dB). (j) TDLRSTV (31.49 dB).
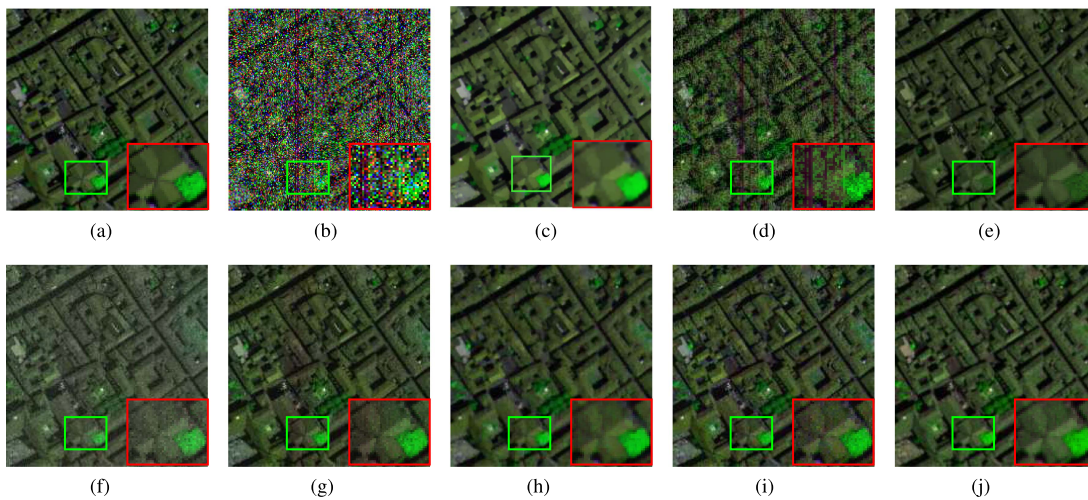

Fig. 6. Recovery performance comparison on the Pavia Centre data by E3DTV, LRTV, BM4D, NAILRMA, LRMR, LRTDTV, SSTV, and the proposed TDLRSTV. The noise level: Gaussian noise [with 0 mean and variance random selected from (0.1, 0.2)] and sparse pepper-and-salt noise [with a percentage random selected from (0.1, 0.2)] are added for all bands, i.e., the case 7: $p = (0.1, 0.2), g = (0.1, 0.2)$, deadline for bands $54 : 74$, stripe for bands $54 : 64$. The color image is composed of bands 31, 61, and 9 for the red, green, and blue channels, respectively. (a) Original image. (b) Noise image (11.17 dB). (c) E3DTV (31.21 dB). (d) LRTV (31.16 dB). (e) BM4D (29.31 dB). (f) NALRMA (22.09 dB). (g) LRMR (30.21 dB). (h) LRTDTV (31.07 dB). (i) SSTV (30.45 dB). (j) Our (32.63 dB).

1) Case 1, Gaussian noise is added to all bands of the selected data, the mean and variance are set as zero and 0.1, respectively.

2) Case 2, on the basis of case 1, the variance is aggravated to 0.2.

3) Case 3, both Gaussian noise (with 0 mean and 0.05 variance) and sparse pepper-and-salt noise (with a percentage of 0.1) are added for all bands.

4) Case 4, on the basis of case 3, the variance of Gaussian noise and the percentage of sparse pepper-and-salt noise are enhanced to 0.075 and 0.15, respectively.

5) Case 5, with the same noise type as case 4, the variance of Gaussian noise and the percentage of sparse pepper-and-salt noise are further aggravated to 0.1 and 0.2, respectively.

6) Case 6, the Gaussian noise is the same as case 2, in addition, deadlines are added to the 131–160 band of Washington DC mall and the 54–74 band of Pavia, respectively. The number of deadlines varies randomly from 3 to 10, and the width of deadlines varies randomly from 1 to 3; stripes are added to the 111–140 band of Washington DC mall and the 48–58 band of Pavia, respectively, where the number of bands varies randomly between 20 and 40. Here, we focus on vertical stripes, for oblique stripes, one can refer to [60] and [61].

7) Case 7, Gaussian noise with zero mean and variance varies randomly from (0, 0.2) [(0.1, 0.2) for Pavia] for all bands, sparse pepper-and-salt noise with percentage varies randomly from (0, 0.2) [(0.1, 0.2) for Pavia] for all
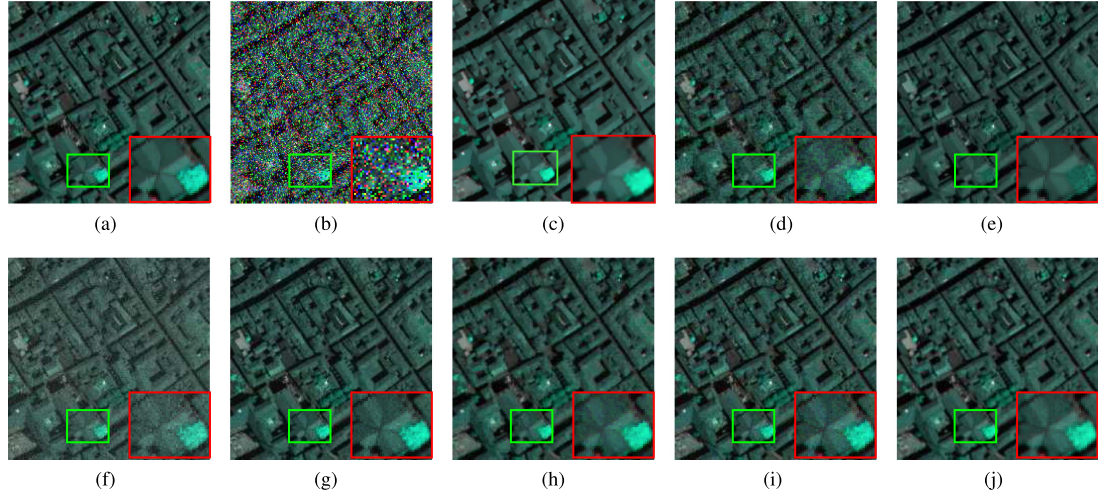
Fig. 7. Recovery performance comparison on the Pavia Centre data by E3DTV, LRTV, BM4D, NAILRMA, LRMR, LRTDTV, SSTV, and the proposed TDLRSTV. The noise level: Gaussian noise (with 0 mean and 0.1 variance) and sparse pepper-and-salt noise (with a percentage of 0.2) are added for all bands, i.e., $P = 0.2$, $G = 0.2$. The color image is composed of bands 14, 77, and 58 for the red, green, and blue channels, respectively. (a) Original image. (b) Noisy one (11.18 dB). (c) E3DTV (32.38 dB). (d) LRTV (29.38 dB). (e) BM4D (28.52 dB). (f) NALRMA (21.87 dB). (g) LRMR (30.77 dB). (h) LRTDTV (31.02 dB). (i) SSTV (31.31 dB). (j) TDLRSTV (33.10 dB).

TABLE I
QUANTITATIVE EVALUATION RESULTS OF THE DIFFERENT DENOISING METHODS WITH THE SIMULATED NOISE IN CASES 1–9 ON WASHINGTON DC MALL DATASET (THE BOLD ONE IS THE BEST ONE)

Noise case	Level	PQIs	Noisy	LRTA	LRTV	BM4D	NAILRMA	LRMR	LRTDTV	SSTV	E3DTV	Ours
Case 1	G=0.1	PSNR	20.001	33.289	33.938	31.795	37.109	34.931	34.035	32.324	32.639	**36.627**
		SSIM	0.339	0.92	0.901	0.903	0.942	0.925	0.916	0.866	0.818	**0.943**
		FSIM	0.662	0.956	0.933	0.936	0.97	0.948	0.942	0.93	0.942	**0.967**
		ERGAS	425.199	86.098	84.529	104.339	55.119	71.889	82.903	110.015	146.350	**60.245**
		SAM	0.357	0.063	0.06	0.074	**0.046**	0.059	0.065	0.089	0.130	0.05
Case 2	G=0.2	PSNR	13.98	29.198	30.664	28.269	**32.486**	30.253	30.872	27.721	30.503	32.415
		SSIM	0.139	0.83	0.813	0.815	**0.862**	0.821	0.842	0.705	0.774	0.861
		FSIM	0.482	0.909	0.872	0.876	**0.928**	0.899	0.903	0.852	0.919	0.923
		ERGAS	850.399	136.107	121.66	153.445	**92.835**	120.515	120.088	181.394	179.659	96.695
		SAM	0.636	0.101	0.092	0.112	**0.077**	0.101	0.096	0.143	0.160	0.082
Case 3	G=0.05 P=0.1	PSNR	14.234	36.577	36.594	35.314	27.258	37.041	36.486	35.876	35.346	**38.781**
		SSIM	0.195	0.962	0.945	0.952	0.808	0.952	0.951	0.937	0.897	**0.968**
		FSIM	0.599	0.978	0.964	0.969	0.926	0.972	0.971	0.965	0.968	**0.983**
		ERGAS	867.536	60.581	62.391	71.652	199.283	59.042	62.301	76.999	134.756	**47.085**
		SAM	0.598	0.042	0.042	0.049	0.145	0.047	0.048	0.063	0.123	**0.038**
Case 4	G=0.075 P=0.15	PSNR	12.387	33.968	34.186	32.802	24.127	33.926	34.318	33.22	33.514	**36.404**
		SSIM	0.122	0.931	0.908	0.923	0.724	0.913	0.92	0.893	0.864	**0.942**
		FSIM	0.514	0.962	0.938	0.949	0.893	0.952	0.944	0.919	0.955	**0.968**
		ERGAS	1070.64	80.096	82.94	93.325	297.986	83.734	80.374	98.23	148.466	**61.431**
		SAM	0.689	0.057	0.057	0.065	0.211	0.067	0.063	0.08	0.136	**0.051**
Case 5	G=0.1 P=0.2	PSNR	11.068	31.926	32.343	31.014	21.839	31.583	32.61	31.138	31.733	**34.684**
		SSIM	0.085	0.896	0.87	0.893	0.647	0.867	0.887	0.841	0.815	**0.915**
		FSIM	0.457	0.944	0.912	0.929	0.863	0.927	0.93	0.919	0.934	**0.952**
		ERGAS	1243.266	100.259	101.336	113.16	397.968	108.636	98.449	121.489	165.961	**74.45**
		SAM	0.753	0.072	0.069	0.08	0.272	0.088	0.078	0.098	0.150	**0.063**
Case 6	G=0.2 Deadline=131:160 Stripe=111:140	PSNR	13.95	29.076	30.738	28.212	32.295	30.069	30.839	27.641	30.377	**32.878**
		SSIM	0.138	0.828	0.82	0.814	0.861	0.818	0.843	0.703	0.767	**0.881**
		FSIM	0.481	0.909	0.875	0.875	0.927	0.898	0.902	0.852	0.917	**0.932**
		ERGAS	853.148	138.063	127.715	154.822	95.051	123.604	122.056	182.814	181.255	**94.21**
		SAM	0.638	0.101	0.095	0.112	**0.079**	0.103	0.098	0.144	0.161	0.08
Case 7	G=(0,0.2) P=(0,0.2) Deadline=131:160 Stripe=111:140	PSNR	13.645	33.403	33.46	31.965	25.635	32.563	33.899	32.52	32.465	**35.22**
		SSIM	0.165	0.93	0.891	0.916	0.761	0.886	0.913	0.881	0.825	**0.933**
		FSIM	0.54	0.959	0.927	0.944	0.906	0.936	0.947	0.938	0.941	**0.962**
		ERGAS	971.828	89.598	97.423	102.326	276.556	99.8	89.609	103.511	174.859	**80.96**
		SAM	0.652	**0.064**	0.075	0.071	0.197	0.082	0.073	0.086	0.144	0.069
Case 8	G=0.15 P=0.2 Deadline=131:160 Stripe=111:140	PSNR	10.665	29.274	30.172	28.707	21.089	29.069	30.631	28.552	29.873	**32.441**
		SSIM	0.072	0.837	0.809	0.838	0.612	0.796	0.838	0.751	0.731	**0.874**
		FSIM	0.43	0.914	0.872	0.893	0.847	0.889	0.9	0.878	0.899	**0.929**
		ERGAS	1288.726	134.921	128.901	146.256	441.014	143.18	124.861	160.407	192.961	**95.866**
		SAM	0.772	0.096	0.092	0.102	0.296	0.117	0.097	0.127	0.171	**0.083**
Case 9	G=0.2 P=0.2 Deadline=131:160 Stripe=111:140	PSNR	10.212	27.416	28.794	27.061	20.242	27.551	29.255	26.739	28.641	**30.815**
		SSIM	0.061	0.785	0.755	0.787	0.578	0.74	0.792	0.671	0.697	**0.835**
		FSIM	0.408	0.887	0.837	0.858	0.834	0.861	0.874	0.84	0.886	**0.908**
		ERGAS	1344.758	166.394	148.07	175.666	492.804	168.475	145.641	196.318	212.321	**115.867**
		SAM	0.791	0.116	0.108	0.121	0.324	0.139	0.114	0.152	0.188	**0.101**

TABLE II
QUANTITATIVE EVALUATION RESULTS OF THE DIFFERENT DENOISING METHODS WITH THE SIMULATED NOISE IN CASES 1–9 ON PAVIA DATASET (THE BOLD ONE IS THE BEST ONE)

Noise case	Level	PQIs	Noisy	LRTA	LRTV	BM4D	NAILRMA	LRMR	LRTDTV	SSTV	E3DTV	Ours
Case 1	G=0.1	PSNR	20.001	31.02	33.234	30.99	**35.19**8	33.748	33.26	33.434	33.781	35.187
		SSIM	0.436	0.929	0.916	0.932	**0.952**	0.942	0.926	0.927	0.911	0.951
		FSIM	0.722	0.958	0.949	0.956	**0.972**	0.962	0.953	0.957	0.958	0.968
		ERGAS	368.912	104.831	89.259	104.88	65.422	78.364	80.014	80.014	79.686	**64.881**
		SAM	0.548	0.127	0.128	0.098	0.107	0.124	0.109	0.146	**0.091**	0.105
Case 2	G=0.2	PSNR	13.98	26.841	29.133	27.07	30.41	29.192	29.554	28.007	30.177	**30.87**
		SSIM	0.182	0.838	0.83	0.857	**0.879**	0.854	0.841	0.801	0.823	0.876
		FSIM	0.546	0.914	0.896	0.91	0.93	0.916	0.903	0.892	0.912	**0.923**
		ERGAS	737.824	167.054	144.929	162.526	111.83	128.298	122.327	149.419	118.402	**107.545**
		SAM	0.828	0.183	0.207	0.125	0.161	0.191	0.152	0.239	**0.119**	0.168
Case 3	G=0.05 P=0.1	PSNR	14.29	34.101	36.289	34.096	26.891	36.385	36.128	**37.771**	36.349	37.352
		SSIM	0.247	0.965	0.962	0.967	0.846	0.967	0.962	0.971	0.948	**0.973**
		FSIM	0.665	0.978	0.975	0.978	0.925	0.979	0.976	**0.984**	0.976	0.983
		ERGAS	717.692	75.447	59.183	75.13	168.129	57.436	57.449	**48.403**	60.937	50.018
		SAM	0.704	0.088	0.094	0.077	0.13	0.084	0.083	0.077	0.078	**0.072**
Case 4	G=0.075 P=0.15	PSNR	12.412	31.441	33.686	31.531	23.947	33.339	33.752	34.403	34.314	**35.274**
		SSIM	0.154	0.938	0.931	0.944	0.773	0.937	0.936	0.94	0.922	**0.955**
		FSIM	0.575	0.963	0.956	0.963	0.898	0.962	0.958	0.969	0.963	**0.972**
		ERGAS	890.259	101.073	82.052	99.823	236.001	80.798	76.2	71.321	75.419	**64.003**
		SAM	0.77	0.111	0.126	0.093	0.147	0.105	0.11	0.101	0.089	**0.089**
Case 5	G=0.1 P=0.2	PSNR	11.082	29.404	31.57	29.628	21.724	31.166	31.67	31.786	32.533	**33.41**
		SSIM	0.105	0.905	0.896	0.919	0.701	0.902	0.902	0.898	0.889	**0.93**
		FSIM	0.514	0.947	0.935	0.947	0.872	0.944	0.937	0.95	0.946	**0.957**
		ERGAS	1037.013	126.62	105.887	123.37	305.688	102.759	96.904	96.406	91.619	**79.551**
		SAM	0.809	0.128	0.156	0.106	0.16	0.121	0.134	0.125	0.108	**0.105**
Case 6	G=0.2 Dead line=54:74 Stripe=54:64	PSNR	13.91	26.521	28.655	26.729	30.193	28.965	29.295	27.792	29.991	**30.553**
		SSIM	0.178	0.834	0.823	0.854	0.877	0.851	0.836	0.797	0.820	**0.884**
		FSIM	0.543	0.913	0.89	0.909	**0.929**	0.915	0.9	0.891	0.910	0.927
		ERGAS	742.599	174.279	153.902	169.729	114.464	131.541	127.949	152.421	120.715	**114.408**
		SAM	0.837	0.187	0.232	0.126	0.165	0.198	0.17	0.248	**0.120**	0.18
Case 7	G=(0.1,0.2) P=(0.1,0.2) Deadline=54:74 Stripe=54:64	PSNR	11.62	27.349	29.594	27.748	22.5	29.369	29.864	29.395	30.696	**31.05**
		SSIM	0.115	0.865	0.843	0.894	0.716	0.863	0.856	0.843	0.845	**0.897**
		FSIM	0.517	0.93	0.905	0.934	0.873	0.925	0.912	0.924	0.922	**0.937**
		ERGAS	982.617	159.906	150.144	152.46	284.596	125.431	119.332	127.077	111.540	115.822
		SAM	0.806	0.145	0.222	0.118	0.172	0.139	0.143	0.157	**0.112**	0.165
Case 8	G=0.15 P=0.2 Deadline=54:74 Stripe=54:64	PSNR	10.666	26.684	28.908	27.002	21.082	28.683	29.042	28.51	30.317	**30.78**
		SSIM	0.087	0.844	0.83	0.872	0.663	0.843	0.837	0.818	0.834	**0.882**
		FSIM	0.485	0.896	0.896	0.92	0.856	0.917	0.899	0.913	0.916	**0.931**
		ERGAS	1085.555	172.021	147.64	165.688	331.455	135.095	131.268	139.649	116.321	**109.451**
		SAM	0.827	0.146	0.205	0.12	0.173	0.144	0.164	0.169	**0.117**	0.142
Case 9	G=0.2 P=0.2 Deadline=54:74 Stripe=54:64	PSNR	10.227	24.819	27.281	25.185	20.202	27.053	27.702	26.369	28.674	**29.13**
		SSIM	0.073	0.784	0.774	0.824	0.626	0.784	0.789	0.74	0.775	**0.849**
		FSIM	0.463	0.884	0.868	0.892	0.842	0.893	0.873	0.878	0.886	**0.911**
		ERGAS	1140.084	211.928	167.908	202.9	367.514	162.357	151.926	178.448	138.460	**134.873**
		SAM	0.835	0.156	0.215	0.129	0.179	0.158	0.175	0.202	**0.126**	0.173

bands. In addition, the deadlines and stripes in case 6 are also added.

8) Case 8, deadline and stripe are the same as case 6 while all the bands are added with the same Gaussian noise (variance of 0.15) and sparse pepper-and-salt noise (percentage of 0.2).

9) Case 9, the types of noise are the same as case 8 but the variance of Gaussian noise is aggravated to 0.2.

Visual comparison: To visually illustrate the denoising performance of the proposed LRSTV, in two different noise situations, for the Washington DC Mall and Pavia datasets, we have selected three bands to synthesize a pseudocolor image, as shown in Figs. 5, 6, and 7. In the figures, the red demarcated window is the magnified area of the area marked by the green demarcated window. From the magnified area, one can clearly see that compared with other competing methods, the proposed method effectively removes the noise while recovering the tiny details and textures.

Quantitative comparison: For Washington DC Mall and Pavia, Tables I and II list the five quantitative evaluation index values (PQIs) of all competing methods. Bold shows the optimal PSNR, SSIM, FSIM, ERGAS, and SAM values. The following observations can be obtained from the table. First of all, under most noise conditions, the proposed LRSTV always achieves the best performance among the five evaluation indicators, which fully proves the effectiveness of LRSTV for HSI denoising tasks. Second, for the mixed noise in Washington DC Mall, as the noise level increases, the advantages of our method over other methods become more obvious. One can observe that when the Gaussian noise variance is 0.2, the proposed method almost exceeds 2.2 dB than LRTDTV. In addition, we took four noise cases as an example, and plotted the PSNR and SSIM values of each band, as shown in Fig. 8. From the figure, one can see that the PSNR value and SSIM value of most bands obtained by the proposed model are significantly higher than other methods. In Fig. 8, it is important to highlight that the original 39th band, which serves
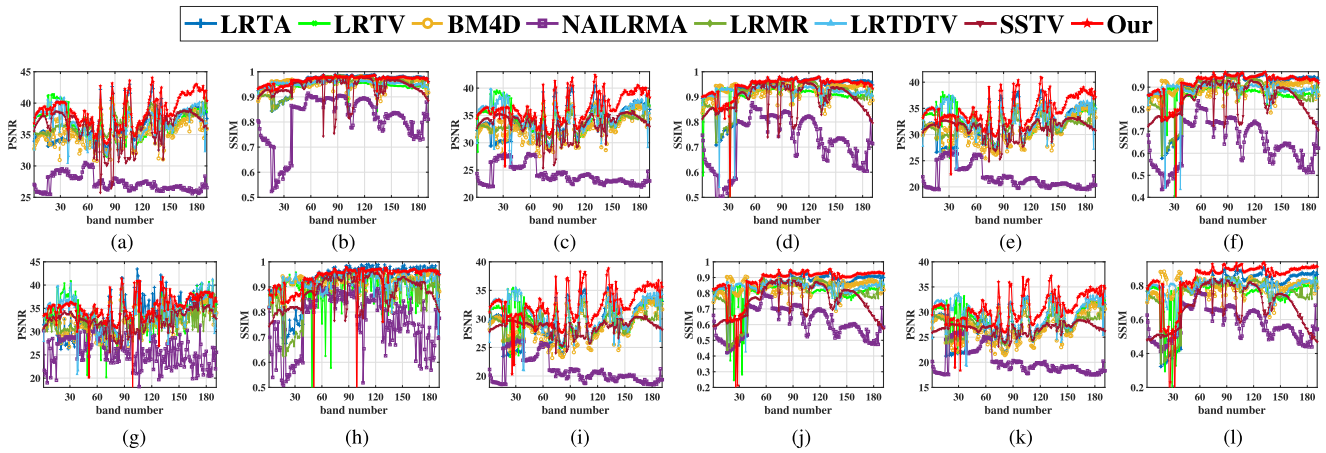
Fig. 8. Comparison of quantitative evaluation index values, PSNR and SSIM, of each band on the Washington DC Mall data by LRTA, LRTV, BM4D, NAILRMA, LRMR, LRTDTV, SSTV, and the proposed TDLRSTV. (a) Case 3. (b) Case 3. (c) Case 6. (d) Case 6. (e) Case 7. (f) Case 7. (g) Case 9. (h) Case 9. (i) Case 8. (j) Case 8. (k) Case 9. (l) Case 9.
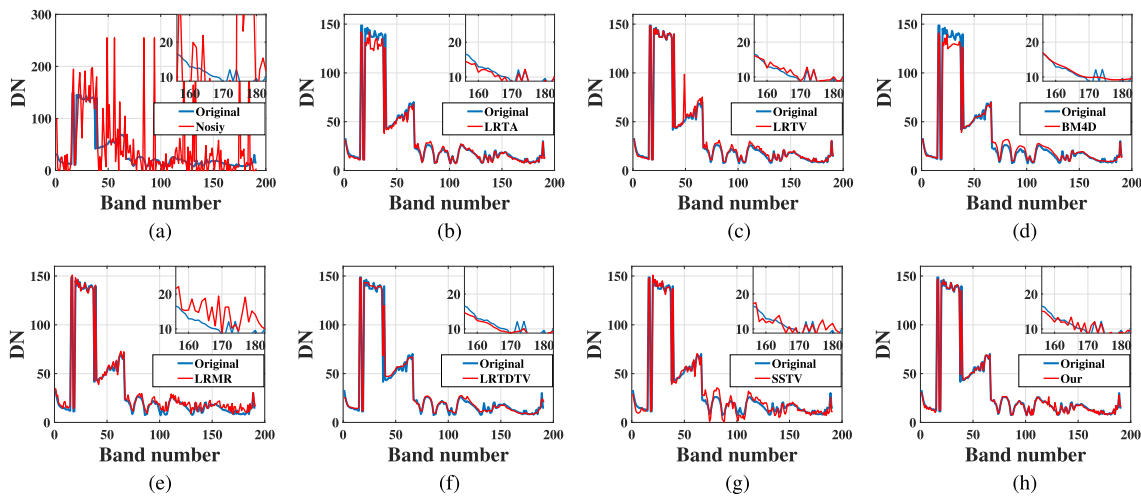

Fig. 9. Reflectance of the spatial pixel of Washington DC Mall in (21,140) under noise case 9. (a) Noisy image. (b) LRTA. (c) LRTV. (d) BM4D. (e) LRMR. (f) LRTDTV. (g) SSTV. (h) TDLRSTV (Our).

as the ground truth for computing PSNR and SSIM, exhibits poor image quality. Consequently, several tested models demonstrate a significant decrease in both PSNR and SSIM scores for this particular band.

To further assess and compare the performance of the tested algorithms, Figs. 9 and 10 show the spectral characteristics of the pixels (21, 140) of Washington DC Mall and (33, 44) of Pavia before and after the denoising. Combining the ERGAS and SAM values in Tables I and II, one can see that among all competing methods, the HSI recovered by the proposed LRSTV method has the spectral characteristics closest to the original clean HSI.

Another interesting observation is that the proposed LRSTV based on low rank and sparseness can obtain better results than the classic SSTV based on sparseness alone and LRTDTV that combines tensor decomposition and SSTV. This result demonstrates the effectiveness of a sparseness criterion combining low-rank and gradient sparsity in HSI processing.

C. Real HSI Data Experiments

Finally, we apply the proposed TDLRSTV to datasets with realistic noise, i.e., HYDICE urban[1] and the AVIRIS Indian Pines [40] to verify the robustness of the algorithms. Figs. 11 and 12 show the recovered two kinds of HSI by using different tested algorithms. From the figures, one can see that TDLRSTV can provide better results than LRTDTV and SSTV, and again with more details be preserved. The horizontal mean profiles of the band 218 of AVIRIS Indian Pine before and after restoration are shown in Fig. 13, where one can see that TDLRSTV provides results with most stable horizontal mean profile curves. Furthermore, Table III provides a blind image quality metric [62], which is based on quality-sensitive feature learning. As one can see that TDLRSTV produces the best (the lowest)

[1]https://engineering.purdue.edu/~biehl/MultiSpec/hyperspectral.html
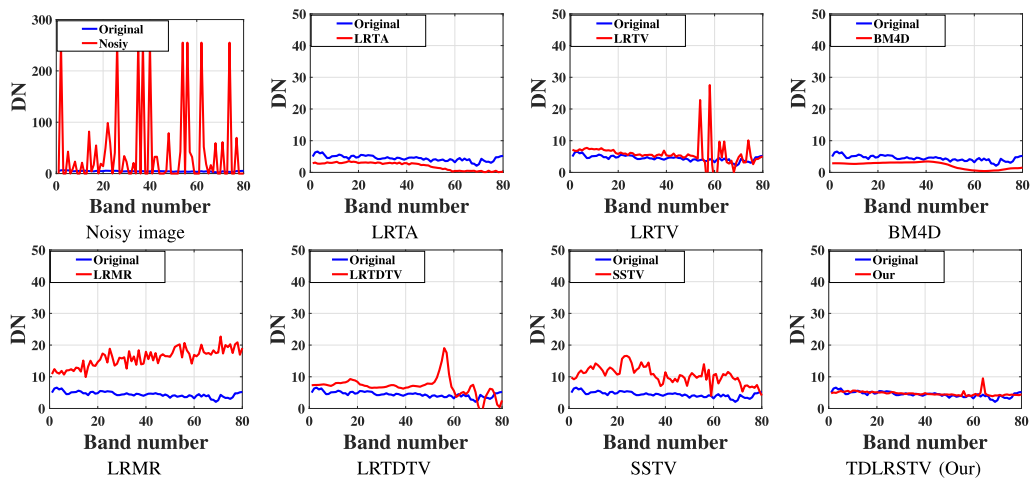
Fig. 10. Reflectance comparison of the spatial pixel of Pavia in (33, 44) with noise Case 9.
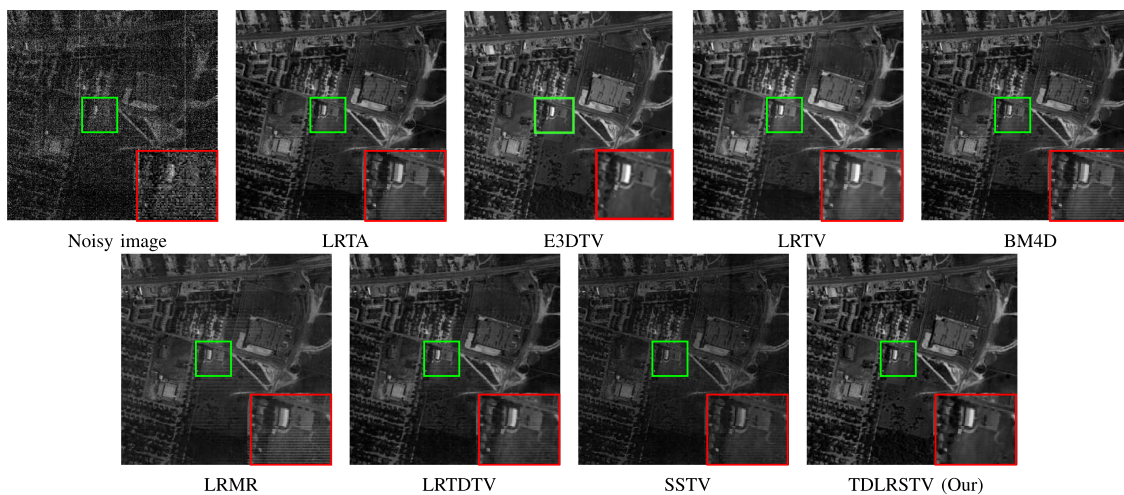

Fig. 11. Recovery performance comparison on the HYDICE Urban data. The noise is real noise, and the original noisy image is band 207.
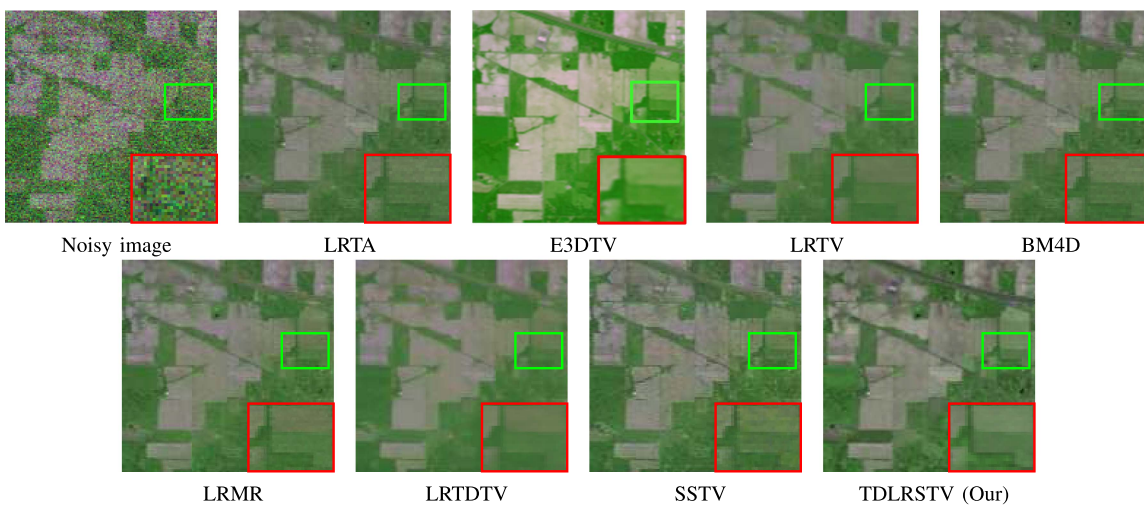

Fig. 12. Recovery performance comparison on the AVIRIS Indian Pines data. The noise is real noise, the color image (R: 164, G: 150, B: 218).
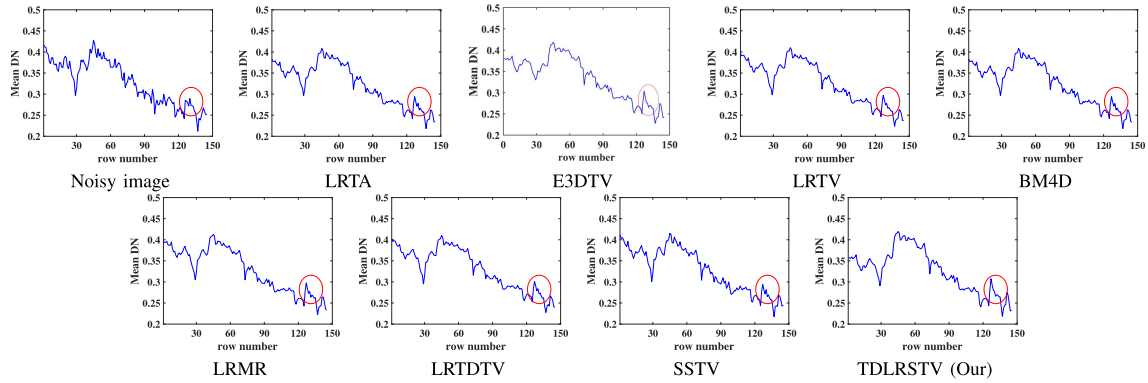
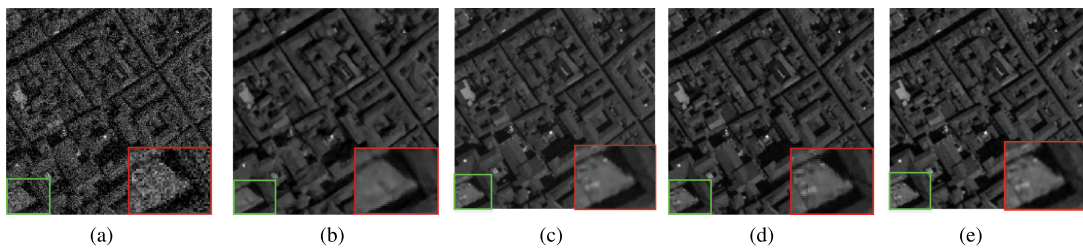Fig. 13.   Horizontal mean profiles comparison on the AVIRIS Indian Pines data, the real noisy image is band 218.

Fig. 14.   Comparison with deep learning, deep unrolling, PnP, and group-sparsity-based methods under noise case $\mathcal{N}(0, 0.1)$. (a) Noisy image. (b) FFDNet. (c) FGSLR. (d) DPLRTA. (e) TDLRSTV.

TABLE III
BLIND HSI QUALITY ASSESSMENT ON THE INDIAN PINES IMAGE

Model	LRMR	LRTDTV	E3DTV	SSTV	TDLRSTV
Score	17.04	16.01	16.05	18.95	15.88
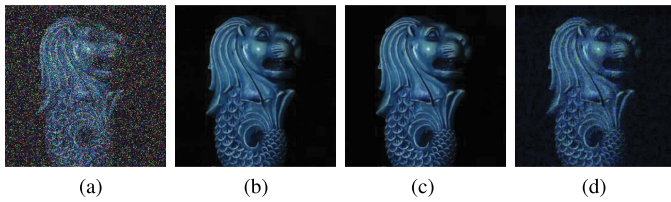
Fig. 15.   Comparison with deep-learning-based methods on the KAIST dataset under noise case $\mathcal{N}(0, 0.2)$. (a) Noisy Image. (b) SERT. (c) DNA-Net. (d) TDLRSTV.
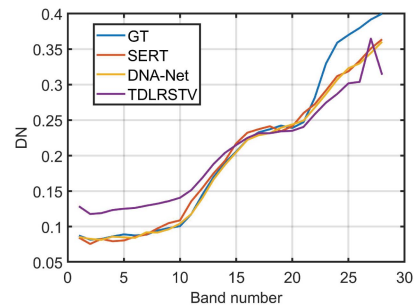

Fig. 16.   Recovered spectrum compared with deep-learning-based methods for the spatial pixel located at (100, 120) in the KAIST dataset, as illustrated in Fig. 15.

score, further demonstrating the superiority of the proposed model.

D. Comparison With Deep Learning and Group Sparsity

Considering the current research landscape in HSI processing, it is imperative to include a comparison with deep learning and group-sparsity-based methods. In this section, the proposed model is evaluated against the following models: PnP and deep prior-based HSI denoising model DPLRTA [20], end-to-end network FFDNet [54], transformer-based SERT [55], deep unrolling-based DNA-Net [56], and group-sparsity-based FGSLR [63].

To ensure a fair comparison, the same noise cases as those employed in the original paper of DPLRTA are implemented, specifically Gaussian noise with zero mean and variances of 0.1 and 0.2. Table IV presents the PSNR, SSIM, FSIM, and ERGAS metrics for the models on the Pavia dataset. The results demonstrate that the proposed model achieves superior PSNR and ERGAS performance under both noise cases.

Fig. 14 showcases the denoised bands on the Pavia dataset while Fig. 15 illustrates the denoised bands on the KAIST dataset [64]. It can be observed that both the proposed model and DPLRTA effectively denoise the images. Since the PSNR difference is less than 2 dB, the denoised bands of DPLRTA and the proposed method exhibit negligible discrepancies. However,
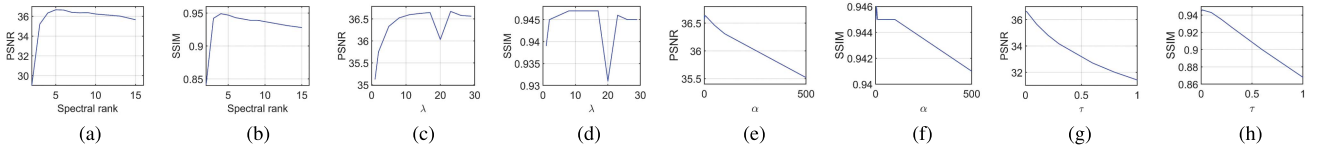
Fig. 17. Sensitivity analysis of parameter: Spectral rank, λ α and τ. (a) PSNR value versus the spectral rank. (b) SSIM value versus the spectral rank. (c) PSNR value versus λ. (d) SSIM value versus λ. (e) PSNR value versus α. (f) SSIM value versus α. (g) PSNR value versus τ. (h) SSIM value versus τ.

TABLE IV
QUANTITATIVE EVALUATION OF DEEP-LEARNING- AND
GROUP-SPARSITY-BASED METHODS AND THE PROPOSED MODEL IN DIFFERENT
NOISE CASES

Noise level	PQI	FFDNet	FGSLR	DPLRTA	TDLRSTV
	PSNR	28.447	35.139	34.976	**35.187**
	SSIM	0.817	0.933	0.950	**0.951**
$\mathcal{N}(0, 0.1)$	FSIM	0.888	**0.971**	0.970	0.968
	ERGAS	137.825	64.978	68.118	**64.881**
	PSNR	25.401	30.849	30.759	**30.870**
	SSIM	0.676	0.854	**0.890**	0.876
$\mathcal{N}(0, 0.2)$	FSIM	0.814	**0.935**	**0.935**	0.923
	ERGAS	195.636	107.713	109.602	**107.545**

The boldface values denote the best value.

both outperform FFDNet. Furthermore, Fig. 16 demonstrates the recovered spectrum compared to deep-learning-based methods for the spatial pixel at coordinates (100, 120) in the KAIST dataset. The results indicate that TDLRSTV achieves comparable spectral accuracy to SERT and DNA-Net.

E. Discussion

This article introduces a novel approach for regularizing HSI reconstruction. The proposed method incorporates a prior regularization term that effectively captures the low rankness and smoothness characteristics of the gradient map. By integrating this regularizer into an iteration-based HSI reconstruction model, we demonstrate its effectiveness by combining it with Tucker decomposition for HSI denoising. To evaluate the performance of the proposed TDLRSTV, we conduct comprehensive comparisons with state-of-the-art methods on both simulated and real datasets. Additionally, we analyze various aspects to further assess the effectiveness and efficiency of TDLRSTV. These aspects include sensitivity analysis of the parameters, convergence analysis, evaluation of the running time, and investigation of the component effects within the proposed model.

1) Sensitivity Analysis of Parameter: There are three parameters used to trade off the regularization terms in the proposed TDLRSTV, i.e., τ, λ, and α. λ is used to trade off the effect of sparsity term $\|\mathcal{S}\|_1$, it can be set as $\lambda = C/\sqrt{MN}$ (M, N is the spatial size of underlying HSI) [42], which is a constant that needs to be tuned manually, Fig. 17(c) and (d) shows the sensitivity of λ. α is used to trade off the low-rank term in LRSTV, τ is the parameter used to control the effect of sparsity of gradient maps, Fig. 17(e), (f) and (g), (h) shows the sensitivity of α and τ, respectively. Besides, the Tucker rank (r_1, r_2, r_3) involved in the low-rank Tucker decomposition is also a sensitive parameter. We set the spatial Tucker rank as follows: r_1 is set
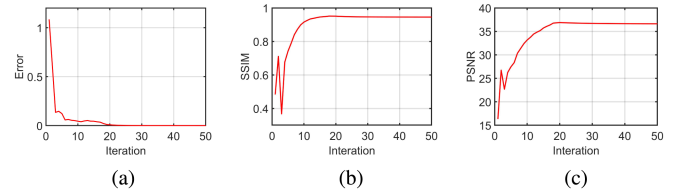

Fig. 18. Relative error, MSSIM, and MPSNR value versus the iteration number of TDLRSTV. (a) Change in the relative error value. (b) Change in the MSSIM value. (c) Change in the MPSNR value.

TABLE V
CPU RUNNING TIME (IN SECONDS) OF ALL THE TESTED MODELS

Data	LRMR	LRTDTV	E3DTV	SSTV	TDLRSTV
Pavia	55.11	47.50	14.97	101.17	76.91
DC	159.07	172.17	66.19	421.09	331.62

to 0.8 times the vertical spatial size and r_2 to 0.8 times the horizontal spatial size [40], and tune r_3 based on the HySime algorithm [45]. Fig. 17(a) and (b) shows the change of PSNR and SSIM values versus the change of spectral rank r_3. Here, we set the spectral rank as the one corresponding to the best PSNR or SSIM.

2) Convergence of the TDLRSTV-Based Algorithm: To show the convergence of the proposed TDLRSTV, Fig. 18 shows the change of relative error, MSSIM, and MPSNR as iteration increases from 1 to 50. In Fig. 18, one can see that the relative error, SSIM, and PSNR all converge to fixed values, which means that the proposed algorithm is robust enough to be further used in real application.

3) Running Time Analysis: Table V provides the running time of all the tested algorithms, which are implemented on the Pavia dataset. One can observe that matrix-based models, e.g., LRMR and SSTV, are faster than tensor-based models but the gap is not very big. This is due to the fact that matrix-based models usually unfold the 3-D HSI into 2-D matrix, which reduces the subsequent computation but loses the 3-D structure of the original HSI tensor. For the tensor-based metrics, they model the 3-D HSI into a third-order tensor directly, and do not lose any structure information but the complexity of 3-D data is higher than 2-D case.

4) Ablation Experiment: In this section, we discuss the effect of the low-rank and sparseness of the gradient map. Table VI provides the comparison of the PSNR, SSIM with different tradeoffs of the two terms. One can observe that introducing low rankness for gradient improves both the PSNR and SSIM.

TABLE VI
PSNR, SSIM OF THE ABLATION OF THE LOW-RANK AND SPARSENESS OF THE GRADIENT MAP

PQIs	Sparse	Pavia Low-Rank	Sparse + Low-Rank
PSNR	32.6	33.95	34.68
SSIM	0.89	0.90	0.91

By undertaking these analyses, we aim to provide a thorough understanding of the performance, efficiency, and underlying characteristics of TDLRSTV in HSI reconstruction and denoising tasks.

V. CONCLUSION

In conclusion, we have proposed a novel TV regularization technique, LRSTV, for HS image restoration, which explicitly represents the low-rank and sparsity of the gradient map in the transform domain using the tensor L_1-norm and the convex envelope of the average rank. By doing so, we have overcome the obstacles of traditional SSTV, which cannot retain the correlation of the spatial–spectral structure of the gradient map and cannot cope with high noise intensity tasks. Furthermore, we have demonstrated that the gradient map of HSI exhibits both sparsity and low rankness, which enhances the restoration accuracy. The proposed LRSTV has been embedded into the HSI denoising model, and excellent results have been achieved on both simulation and real datasets. Further work will involve designing a better low-rank regularization term or training a denoising network and combining it with the proposed LRSTV to improve the performance of the HSI restoration model.

REFERENCES

[1] Y. Xu, Z. Wu, F. Xiao, T. Zhan, and Z. Wei, "A target detection method based on low-rank regularized least squares model for hyperspectral images," *IEEE Geosci. Remote Sens. Lett.*, vol. 13, no. 8, pp. 1129–1133, Aug. 2016.

[2] A. F. Goetz, "Three decades of hyperspectral remote sensing of the earth: A personal view," *Remote Sens. Environ.*, vol. 113, pp. S5–S16, 2009.

[3] J. Peng, Q. Xie, Q. Zhao, Y. Wang, L. Yee, and D. Meng, "Enhanced 3DTV regularization and its applications on HSI denoising and compressed sensing," *IEEE Trans. Image Process.*, vol. 29, pp. 7889–7903, 2020.

[4] Y. Zhang, A. Duijster, and P. Scheunders, "A Bayesian restoration approach for hyperspectral images," *IEEE Trans. Geosci. Remote Sens.*, vol. 50, no. 9, pp. 3453–3462, 2012.

[5] J. Xue, Y. Zhao, S. Huang, W. Liao, J. C.-W. Chan, and S. G. Kong, "Multilayer sparsity-based tensor decomposition for low-rank tensor completion," *IEEE Trans. Neural Netw.*, vol. 33, no. 11, pp. 6916–6930, Nov. 2022.

[6] H. Wang, Y. Li, Y. Cen, and Z. He, "Multi-matrices low-rank decomposition with structural smoothness for image denoising," *IEEE Trans. Circuits Syst. Video Technol.*, vol. 30, no. 2, pp. 349–361, Feb. 2020.

[7] T. Xie, S. Li, L. Fang, and L. Liu, "Tensor completion via nonlocal low-rank regularization," *IEEE Trans. Cybern.*, vol. 49, no. 6, pp. 2344–2354, Jun. 2019.

[8] L. Zhuang, X. Fu, M. K. Ng, and J. M. Bioucas-Dias, "Hyperspectral image denoising based on global and nonlocal low-rank factorizations," *IEEE Trans. Geosci. Remote Sens.*, vol. 59, no. 12, pp. 10438–10454, Dec. 2021.

[9] M. Maggioni, V. Katkovnik, K. Egiazarian, and A. Foi, "Nonlocal transform-domain filter for volumetric data denoising and reconstruction," *IEEE Trans. Image Process.*, vol. 22, no. 1, pp. 119–133, Jan. 2013.

[10] H. Zhang, W. He, L. Zhang, H. Shen, and Q. Yuan, "Hyperspectral image restoration using low-rank matrix recovery," *IEEE Trans. Geosci. Remote Sens.*, vol. 52, no. 8, pp. 4729–4743, Aug. 2013.

[11] H. Liu, R. Xiong, D. Liu, S. Ma, F. Wu, and W. Gao, "Image denoising via low rank regularization exploiting intra and inter patch correlation," *IEEE Trans. Circuits Syst. Video Technol.*, vol. 28, no. 12, pp. 3321–3332, Dec. 2018.

[12] Y. Chen, Y. Guo, Y. Wang, D. Wang, C. Peng, and G. He, "Denoising of hyperspectral images using nonconvex low rank matrix approximation," *IEEE Trans. Geosci. Remote Sens.*, vol. 55, no. 9, pp. 5366–5380, Sep. 2017.

[13] Z. Zha, X. Yuan, B. Wen, J. Zhou, J. Zhang, and C. Zhu, "From rank estimation to rank approximation: Rank residual constraint for image restoration," *IEEE Trans. Image Process.*, vol. 29, pp. 3254–3269, 2020.

[14] Z. Zha, X. Yuan, B. Wen, J. Zhou, J. Zhang, and C. Zhu, "A benchmark for sparse coding: When group sparsity meets rank minimization," *IEEE Trans. Image Process.*, vol. 29, pp. 5094–5109, 2020.

[15] Z. Zha, X. Yuan, B. Wen, J. Zhang, J. Zhou, and C. Zhu, "Image restoration using joint patch-group-based sparse representation," *IEEE Trans. Image Process.*, vol. 29, pp. 7735–7750, 2020.

[16] Z. Zha, X. Yuan, B. Wen, J. Zhou, and C. Zhu, "Group sparsity residual constraint with non-local priors for image restoration," *IEEE Trans. Image Process.*, vol. 29, pp. 8960–8975, 2020.

[17] Z. Zha, B. Wen, X. Yuan, J. Zhou, and C. Zhu, "Image restoration via reconciliation of group sparsity and low-rank models," *IEEE Trans. Image Process.*, vol. 30, pp. 5223–5238, 2021.

[18] Z. Zha, B. Wen, X. Yuan, J. Zhou, C. Zhu, and A. C. Kot, "Low-rankness guided group sparse representation for image restoration," *IEEE Trans. Neural Netw. Learn. Syst.*, early access, Feb. 7, 2022, doi: 10.1109/TNNLS.2022.3144630.

[19] H. Zeng, X. Xie, W. Kong, S. Cui, and J. Ning, "Hyperspectral image denoising via combined non-local self-similarity and local low-rank regularization," *IEEE Access*, vol. 8, pp. 50190–50208, 2020.

[20] H. Zeng, X. Xie, H. Cui, Y. Zhao, and J. Ning, "Hyperspectral image restoration via CNN denoiser prior regularized low-rank tensor recovery," *Comput. Vis. Image Understanding*, vol. 197, 2020, Art. no. 103004.

[21] Y. Chang, L. Yan, X.-L. Zhao, H. Fang, Z. Zhang, and S. Zhong, "Weighted low-rank tensor recovery for hyperspectral image restoration," *IEEE Trans. Cybern.*, vol. 50, no. 11, pp. 4558–4572, Nov. 2020.

[22] J. Xue, Y.-Q. Zhao, Y. Bu, W. Liao, J. C.-W. Chan, and W. Philips, "Spatial-spectral structured sparse low-rank representation for hyperspectral image super-resolution," *IEEE Trans. Image Process.*, vol. 30, pp. 3084–3097, 2021.

[23] H. Zeng, J. Xue, H. Q. Luong, and W. Philips, "Multimodal core tensor factorization and its applications to low-rank tensor completion," *IEEE Trans. Multimedia*, early access, Oct. 25, 2022, doi: 10.1109/TMM.2022.3216746.

[24] H. Zeng, S. Huang, Y. Chen, S. Liu, H. Q. Luong, and W. Philips, "Tensor completion using bilayer multimode low-rank prior and total variation," *IEEE Trans. Neural Netw. Learn. Syst.*, early access, May 17, 2023, doi: 10.1109/TNNLS.2023.3266841.

[25] H. Zeng, X. Xie, H. Cui, Y. Zhao, and J. Ning, "Hyperspectral image restoration via CNN denoiser prior regularized low-rank tensor recovery," *Comput. Vis. Image Understanding*, vol. 197/198, 2020, Art. no. 103004.

[26] H. Zhang, X.-L. Zhao, T.-X. Jiang, M. K. Ng, and T.-Z. Huang, "Multiscale feature tensor train rank minimization for multidimensional image recovery," *IEEE Trans. Cybern.*, vol. 52, no. 12, pp. 13395–13410, Dec. 2022.

[27] Y. Chen, J. Zeng, W. He, X.-L. Zhao, and T.-Z. Huang, "Hyperspectral and multispectral image fusion using factor smoothed tensor ring decomposition," *IEEE Trans. Geosci. Remote Sens.*, vol. 60, 2022, Art. no. 5515417.

[28] J. Xue, Y. Zhao, W. Liao, and J. C.-W. Chan, "Nonlocal low-rank regularized tensor decomposition for hyperspectral image denoising," *IEEE Trans. Geosci. Remote Sens.*, vol. 57, no. 7, pp. 5174–5189, Jul. 2019.

[29] X. Tian, K. Xie, and H. Zhang, "A low-rank tensor decomposition model with factors prior and total variation for impulsive noise removal," *IEEE Trans. Image Process.*, vol. 31, pp. 4776–4789, 2022.

[30] W. Xu, Q. Zhu, N. Qi, and D. Chen, "Deep sparse representation based image restoration with denoising prior," *IEEE Trans. Circuits Syst. Video Technol.*, vol. 32, no. 10, pp. 6530–6542, Oct. 2022.

[31] H. Zeng, X. Xie, and J. Ning, "Hyperspectral image denoising via global spatial-spectral total variation regularized nonconvex local low-rank tensor approximation," *Signal Process.*, vol. 178, 2021, Art. no. 107805.

[32] R. Chartrand, "Exact reconstruction of sparse signals via nonconvex minimization," *IEEE Signal Process. Lett.*, vol. 14, no. 10, pp. 707–710, Oct. 2007.

[33] Y. Lou, T. Zeng, S. Osher, and J. Xin, "A weighted difference of anisotropic and isotropic total variation model for image processing," *SIAM J. Imag. Sci.*, vol. 8, no. 3, pp. 1798–1823, 2015.

[34] K. Bredies, K. Kunisch, and T. Pock, "Total generalized variation," *SIAM J. Imag. Sci.*, vol. 3, no. 3, pp. 492–526, 2010.

[35] P. Li, W. Chen, and M. K. Ng, "Compressive total variation for image reconstruction and restoration," *Comput. Math. Appl.*, vol. 80, no. 5, pp. 874–893, 2020.

[36] Y. Chang, L. Yan, H. Fang, and C. Luo, "Anisotropic spectral-spatial total variation model for multispectral remote sensing image destriping," *IEEE Trans. Image Process.*, vol. 24, no. 6, pp. 1852–1866, Jun. 2015.

[37] H. Zeng, X. Xie, H. Cui, H. Yin, and J. Ning, "Hyperspectral image restoration via global l_{1-2} spatial-spectral total variation regularized local low-rank tensor recovery," *IEEE Trans. Geosci. Remote Sens.*, vol. 59, no. 4, pp. 3309–3325, Apr. 2021.

[38] L. Zhang, Y. Qian, J. Han, P. Duan, and P. Ghamisi, "Mixed noise removal for hyperspectral image with $\{l_{0}\} - \{l_{1-2}\}$ SSTV regularization," *IEEE J. Sel. Topics Appl. Earth Observ. Remote Sens.*, vol. 15, pp. 5371–5387, 2022.

[39] M. Wang, Q. Wang, J. Chanussot, and D. Hong, "L0-l1 hybrid total variation regularization and its applications on hyperspectral image mixed noise removal and compressed sensing," *IEEE Trans. Geosci. Remote Sens.*, vol. 59, no. 9, pp. 7695–7710, Sep. 2021.

[40] Y. Wang, J. Peng, Q. Zhao, Y. Leung, X.-L. Zhao, and D. Meng, "Hyperspectral image restoration via total variation regularized low-rank tensor decomposition," *IEEE J. Sel. Topics Appl. Earth Observ. Remote Sens.*, vol. 11, no. 4, pp. 1227–1243, Apr. 2018.

[41] W. He, H. Zhang, L. Zhang, and H. Shen, "Total-variation-regularized low-rank matrix factorization for hyperspectral image restoration," *IEEE Trans. Geosci. Remote Sens.*, vol. 54, no. 1, pp. 178–188, Jan. 2016.

[42] C. Lu, J. Feng, Y. Chen, W. Liu, Z. Lin, and S. Yan, "Tensor robust principal component analysis with a new tensor nuclear norm," *IEEE Trans. Pattern Anal. Mach. Intell.*, vol. 42, no. 4, pp. 925–938, Apr. 2020.

[43] H. Kong, C. Lu, and Z. Lin, "Tensor Q-rank: New data dependent definition of tensor rank," *Mach. Learn.*, vol. 110, no. 7, pp. 1867–1900, 2021.

[44] C. Lu, J. Feng, Y. Chen, W. Liu, Z. Lin, and S. Yan, "Tensor robust principal component analysis with a new tensor nuclear norm," *IEEE Trans. Pattern Anal. Mach. Intell.*, vol. 42, no. 4, pp. 925–938, Apr. 2020.

[45] J. M. Bioucas-Dias and J. M. Nascimento, "Hyperspectral subspace identification," *IEEE Trans. Geosci. Remote Sens.*, vol. 46, no. 8, pp. 2435–2445, Aug. 2008.

[46] T. G. Kolda and B. W. Bader, "Tensor decompositions and applications," *SIAM Rev.*, vol. 51, no. 3, pp. 455–500, 2009.

[47] Z. Zhang and S. Aeron, "Exact tensor completion using t-SVD," *IEEE Trans. Signal Process.*, vol. 65, no. 6, pp. 1511–1526, Mar. 2017.

[48] 2017. Accessed: Apr. 4, 2018. [Online]. Available: http://www.ehu.es/ccwintco/index.php/Hyperspectral_Remote_Sensing_Scenes/

[49] 2020. Accessed: Apr. 4, 2018. [Online]. Available: https://engineering.purdue.edu/biehl/MultiSpec/hyperspectral.html/

[50] 2017. Accessed: Apr. 4, 2018. [Online]. Available: http://www.tec.army.mil/hypercube/

[51] N. Renard, S. Bourennane, and J. Blanc-Talon, "Denoising and dimensionality reduction using multilinear tools for hyperspectral images," *IEEE Geosci. Remote Sens. Lett.*, vol. 5, no. 2, pp. 138–142, Apr. 2008.

[52] W. He, H. Zhang, L. Zhang, and H. Shen, "Hyperspectral image denoising via noise-adjusted iterative low-rank matrix approximation," *IEEE J. Sel. Topics Appl. Earth Observ. Remote Sens.*, vol. 8, no. 6, pp. 3050–3061, Jun. 2015.

[53] H. Fang, C. Luo, G. Zhou, and X. Wang, "Hyperspectral image deconvolution with a spectral-spatial total variation regularization," *Can. J. Remote Sens.*, vol. 43, no. 4, pp. 384–395, 2017.

[54] K. Zhang, W. Zuo, and L. Zhang, "FFDNet: Toward a fast and flexible solution for CNN-based image denoising," *IEEE Trans. Image Process.*, vol. 27, no. 9, pp. 4608–4622, Sep. 2018.

[55] M. Li, J. Liu, Y. Fu, Y. Zhang, and D. Dou, "Spectral enhanced rectangle transformer for hyperspectral image denoising," in *Proc. IEEE/CVF Conf. Comput. Vis. Pattern Recognit.*, 2023, pp. 5805–5814.

[56] H. Zeng et al., "Degradation-noise-aware deep unfolding transformer for hyperspectral image denoising," 2023, *arXiv:2305.04047*.

[57] L. Zhang, L. Zhang, X. Mou, and D. Zhang, "FSIM: A feature similarity index for image quality assessment," *IEEE Trans. Image Process.*, vol. 20, no. 8, pp. 2378–2386, Aug. 2011.

[58] L. Wald, *Data Fusion: Definitions and Architectures: Fusion of Images of Different Spatial Resolutions*. Paris, France: Les Presses de l'École des Mines, 2002.

[59] O. A. De Carvalho and P. R. Meneses, "Spectral correlation mapper (SCM): An improvement on the spectral angle mapper (SAM)," in *Proc. Summaries 9th JPL Airborne Earth Sci. Workshop*, 2000, vol. 9, Art. no. 2.

[60] J.-L. Wang, T.-Z. Huang, T.-H. Ma, X.-L. Zhao, and Y. Chen, "A sheared low-rank model for oblique stripe removal," *Appl. Math. Comput.*, vol. 360, pp. 167–180, 2019.

[61] S. Ono, T. Miyata, and I. Yamada, "Cartoon-texture image decomposition using blockwise low-rank texture characterization," *IEEE Trans. Image Process.*, vol. 23, no. 3, pp. 1128–1142, Mar. 2014.

[62] J. Yang, Y.-Q. Zhao, C. Yi, and J. C.-W. Chan, "No-reference hyperspectral image quality assessment via quality-sensitive features learning," *Remote Sens.*, vol. 9, no. 4, 2017, Art. no. 305.

[63] Y. Chen, T.-Z. Huang, W. He, X.-L. Zhao, H. Zhang, and J. Zeng, "Hyperspectral image denoising using factor group sparsity-regularized nonconvex low-rank approximation," *IEEE Trans. Geosci. Remote Sens.*, vol. 60, 2021, Art. no. 5515916.

[64] I. Choi, D. S. Jeon, G. Nam, D. Gutierrez, and M. H. Kim, "High-quality hyperspectral reconstruction using a spectral prior," *ACM Trans. Graph.*, vol. 36, no. 6, Nov. 2017, Art. no. 218.

Haijin Zeng (Student Member, IEEE) received the M.S. degree in applied mathematics from Northwest A&F University, Yangling, China, in 2021. He is currently working toward the Ph.D. degree in telecommunications and information processing with imec & Ghent University, Ghent, Belgium.

He has authored or coauthored several research papers in top-tier journals, including IEEE TRANSACTIONS ON NEURAL NETWORKS AND LEARNING SYSTEMS, IEEE TRANSACTIONS ON GEOSCIENCE AND REMOTE SENSING, IEEE TRANSACTIONS ON MULTIMEDIA, IEEE TRANSACTIONS ON COMPUTATIONAL IMAGING, and *Computer Vision and Image Understanding*, on the topics of his research interests, which include image quality improvement, and applications of deep learning and low-rank representation in computational imaging.

Mr. Zeng won the third place in ECCV 2022 Mobile Intelligent Photography and Imaging Challenge.
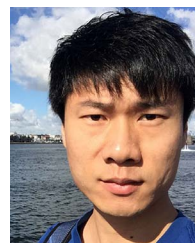
Shaoguang Huang (Member, IEEE) received the M.S. degree in telecommunication and information system from Shandong University, Jinan, China, in 2015, and the Ph.D. degree in computer science engineering from Ghent University, Ghent, Belgium, in 2019.

He is currently an Associate Professor with the School of Computer Science, China University of Geosciences, Wuhan, China. His research interests include image processing, sparse representation, clustering, hyperspectral image analysis, and machine learning.

Dr. Huang is currently a Guest Editor for *Remote Sensing*. He is also a Reviewer of the international journals, including IEEE TRANSACTIONS ON CYBERNETICS, IEEE TRANSACTIONS ON KNOWLEDGE AND DATA ENGINEERING, IEEE TRANSACTIONS ON GEOSCIENCE AND REMOTE SENSING, IEEE TRANSACTIONS ON CIRCUITS AND SYSTEMS FOR VIDEO TECHNOLOGY, IEEE TRANSACTIONS ON BIOMEDICAL CIRCUITS AND SYSTEMS, IEEE GEOSCIENCE AND REMOTE SENSING LETTERS, *Knowledge-Based Systems, Pattern Recognition, Remote Sensing*, and *Computers & Geosciences*.

Yongyong Chen (Member, IEEE) received the B.S. and M.S. degrees in information and computing science from the Shandong University of Science and Technology, Qingdao, China, in 2014 and 2017, respectively, and the Ph.D. degree in computer science from the University of Macau, Macau, in 2020.

He is currently an Assistant Professor with the School of Computer Science and Technology, Harbin Institute of Technology, Shenzhen, China. He has authored or coauthored more than 50 research papers in top-tier journals and conferences, including IEEE TRANSACTIONS ON IMAGE PROCESSING, IEEE TRANSACTIONS ON INFORMATION FORENSICS AND SECURITY, IEEE TRANSACTIONS ON DEPENDABLE AND SECURE COMPUTING, IEEE TRANSACTIONS ON KNOWLEDGE AND DATA ENGINEERING, IEEE TRANSACTIONS ON NEURAL NETWORKS AND LEARNING SYSTEMS, IEEE TRANSACTIONS ON CYBERNETICS, IEEE TRANSACTIONS ON MULTIMEDIA, IEEE TRANSACTIONS ON CIRCUITS AND SYSTEMS FOR VIDEO TECHNOLOGY, IEEE TRANSACTIONS ON GEOSCIENCE AND REMOTE SENSING, IEEE TRANSACTIONS ON COMPUTATIONAL IMAGING, and ACM Multimedia. His research interests include image processing, data mining, and computer vision.

Hiep Luong received the Ph.D. degree in computer science engineering from Ghent University, Ghent, Belgium, in 2009.

He has been a Postdoctoral Researcher and the Project Manager of Image Processing and Interpretation (IPI), an imec Research Group, Ghent University. He is currently a Professor with IPI and leads the UAV Research Centre, Ghent University. His research interests include image and real-time video processing for various fields, such as HDR imaging, (bio) medical imaging, depth and multiview processing, and multisensor fusion for UAV and AR applications.

Wilfried Philips (Senior Member, IEEE) was born in Aalst, Belgium, in 1966. He received the Diploma degree in electrical engineering and the Ph.D. degree in applied sciences from Ghent University, Ghent, Belgium, in 1989 and 1993, respectively.

He is currently a Senior Full Professor with the Department of Telecommunications and Information Processing, Ghent University, where he heads the Image Processing and Interpretation Research Group. He also leads the activities in image processing and sensor fusion within the research institute imec. He is also a Cofounder of the Senso2Me Company, which provides Internet-of-Things solutions for elderly care. His main research interests include image and video quality improvement and estimation, real-time computer vision, and sensor data processing.